Vimentin intermediate filament assembly is a reversible process

Quang D Tran, Valerio Sorichetti, Gerard Pehau-Arnaudet, Martin Lenz, Cécile Leduc

Main Manuscript

Vimentin intermediate filament assembly is a reversible process

Quang D. Tran[a,1], Valerio Sorichetti[b,1], Gerard Pehau-Arnaudet[c,d], Martin Lenz[b,e,2] and Cécile Leduc[a,2]

[a]Université Paris Cité, CNRS, Institut Jacques Monod, F-75013 Paris, France

[b]Université Paris-Saclay, CNRS, Laboratoire de Physique Théorique et Modèles Statistiques (LPTMS), F-91405 Orsay, France

[c]CNRS, Institut Pasteur, F-75015 Paris, France

[d]Ultrastructural BioImaging Platform, Institut Pasteur, F-75015 Paris, France

[e]Physique et Mécanique des Milieux Hétérogènes (PMMH), CNRS, Ecole Supérieure de Physique et de Chimie Industrielles de la Ville de Paris, Paris Science & Lettres Research University, Sorbonne Université, Université Paris Cité, F-75005, Paris, France

[1] equal contributions

[2] To whom correspondence may be addressed: Cécile Leduc and Martin Lenz

Email: cecile.leduc@cnrs.fr and martin.lenz@universite-paris-saclay.fr

Author Contributions: QDT, VS, ML and CL designed research; QDT performed experiments and analyzed data; VS and ML developed the theoretical model; VS performed numerical simulations; GPA performed EM imaging; QDT, VS, ML and CL wrote the paper.

Competing Interest Statement: The authors declare no competing interest.

Classification: Biophysics

Keywords: Intermediate filaments, Vimentin, assembly process, severing/fragmentation

This PDF file includes:

Main Text
Figures 1 to 4

Abstract

Networks of intermediate filaments (IF) need to constantly reorganize to fulfill their functions at different locations within the cell. IF assembly results from end-to-end annealing, which is commonly assumed to be irreversible. By contrast, the mechanisms involved in IF disassembly are far less understood. IF fragmentation has however been observed in many cell types, and it has been suggested that it could be associated with post-translational modifications. In this article, we investigate the contribution of filament fragmentation in the assembly dynamics of type III vimentin IF using a combination of *in vitro* reconstitution, fluorescence imaging, and theoretical modeling. We first show that vimentin assembly at low concentrations results in an equilibrium between filament annealing and fragmentation at time ≥ 24 h. At higher concentration, entanglements kinetically trap the system out of equilibrium, and we show that this trapping is reversible upon dilution. Taking into account both fragmentation and entanglement, we estimated that the mean bond breaking time was ~18 hours Finally, we provide direct evidence through dual color imaging that filament fragmentation and annealing coexist during assembly. By showing that IF fragmentation can occur without cofactors or post-translational-modifications, our study provides a physical understanding of the IF length regulation.

Significance Statement

Vimentin intermediate filaments are a key component of the cytoskeleton and are involved in many cellular functions, such as the regulation of cell shape, migration and division. These functions require cytoskeletal filaments to simultaneously assemble and disassemble throughout the life of the cell. While the mechanisms of intermediate filament assembly have been widely studied, the minimal ingredients underpinning their disassembly are not understood. Here, we demonstrate that vimentin constantly disassembles through filament breakage without the assistance of any other protein or post-translational modification, contrary to common wisdom. Our findings suggest that the dynamic cytoskeletal steady-states observed in cells could be largely shaped by simple physical effects linked to the reversible association of vimentin subunits, combined with dramatic kinetic trapping effects that hinder network reorganization as soon as the filaments become too dense and too long.

Main Text

Introduction

Intermediate filaments (IF), actin filaments and microtubules are the three main components of the cytoskeleton, which controls the mechanical properties and integrity of living cells (1, 2). Cytoplasmic IF networks extend from the cell nucleus to the cell periphery and act in coordination with other types of cytoskeletal filaments to perform common cell functions such as cell migration, division and mechanosensing (3–9). To perform these functions at different locations inside the cell, IFs need to constantly reorganize and remodel their networks. The main drivers of IF dynamics are active transport along F-actin and microtubules (10–16) and a combination of assembly and disassembly (14, 17–20). In the case of vimentin, a type III IF which is the major cytoskeletal component of mesenchymal cells (21), the mechanism responsible for filament assembly has been well characterized and involves longitudinal end-to-end annealing of filaments (14, 18, 22). By contrast, the mechanisms involved in vimentin disassembly are much less understood. Depolymerization events have been shown to be negligible in comparison with filament fragmentation (14), which is also referred to as severing in the literature (14, 17–19). Vimentin fragmentation has been observed in many cell types (14), but it is unclear whether it occurs spontaneously or whether it requires other cues like cofactors or post-translational modifications (20, 23).

In vitro reconstitution experiments using recombinant vimentin have been instrumental to elucidating vimentin assembly. This is commonly divided in three steps: (i) after addition of salt which initiates the assembly, the lateral association of approximately 8 tetramers leads to the formation of 60 nm long unit-length filaments (ULFs) within seconds, (ii) ULFs anneal end-to-end to form extended filaments, (iii) these filaments undergo radial compaction, also referred to as maturation, within 10 to 30 minutes thus giving rise to 10-nm diameter filaments (24–31). Mature filaments then further elongate by end-to-end annealing (29). Spontaneous fragmentation of vimentin has not been previously reported in purified systems reconstituted *in vitro* (30). Based on this experimental evidence, theoretical models of vimentin assembly have consistently neglected the possibility of filament disassembly (27, 31–35). They thus predict unlimited filament assembly without a finite steady-state length, in contrast to other cytoskeletal filaments. Available data however suggest that these assumptions may start to break down at long times (over 4h), where the quantitative accuracy of these models deteriorates (33, 34). Data describing these long time-scales is sparse, however, which contributes to our lack of understanding of filament disassembly.

Here, we investigate the reversibility of vimentin assembly using *in vitro* reconstitution and fluorescence microscopy coupled to theoretical modeling. We first study the assembly of vimentin IFs over long time scales, and observe that filament length gradually reaches saturation. This can be explained quantitatively by taking into account filament disassembly by fragmentation and, at high concentration, entanglement effects. We then provide direct evidence that the assembly process is reversible by demonstrating a progressive decrease of the filament length after dilution. Finally, we show that filament disassembly is triggered by the fragmentation of individual filaments, which occurs concomitantly with end-to-end annealing during the assembly process.

Results

Vimentin filament length reaches a plateau after >24h assembly. To assess whether filament assembly can reach an equilibrium, we monitored the length of recombinant vimentin filaments over a period of more than 24 h after the initiation of assembly. Experiments were performed at 37 °C in a sodium phosphate buffer (2.5 mM, pH 7.0), conditions in which the radial compaction is limited (Fig. S1). We used fluorescently labeled proteins to perform length quantification. We imaged the filaments at multiple time points and multiple concentrations from 0.01 mg.mL^{-1} to 1 mg.mL^{-1} (Fig. 1A) and quantified the mean length for each condition (Fig. 1B). The assembly curves showed that the assembly rate decreased over time and that the mean length reached a plateau at time > 24 h. Using transmission electron microscopy (TEM), we verified that fluorescence labeling had no impact on the existence of the length plateau (Fig. S2). Additionally, we confirmed that the sample mixing methods that we used in our experiments, i.e. pipetting and vortexing, did not impact the estimation of filament mean length (Fig. S3). The existence of a plateau value for the mean length at long time scales suggests that filaments may have reached either an equilibrium involving the simultaneous assembly and disassembly of freely diffusing filaments, or a non-equilibrium (quasi-) steady-state where filaments are so entangled that their diffusion is severely hampered, hindering both assembly and disassembly (see Discussion) (36).

Modeling filaments as diffusing rods undergoing annealing and fragmentation accounts for the time evolution of filament lengths. To model filament growth in the presence of simultaneous assembly and disassembly, we used a mathematical model where our system is represented as a set of filaments of different lengths that randomly anneal end-to-end to form longer filaments, or fragment into smaller filaments. We employed a generalization of the Smoluchowski coagulation equation which takes into account fragmentation (37) (see Supplementary text for details):

$$\frac{dc_k}{dt} = \frac{1}{2}\sum_{i=1}^{k-1}\left(K_{i,k-i}c_i c_{k-i} - F_{i,k-i}c_k\right) - \sum_{i=1}^{\infty}\left(K_{i,k}c_i c_k - F_{i,k}c_{i+k}\right). \qquad (1)$$

Here, c_k is the concentration of filaments of length k (in number of ULFs), $K_{i,j}$ is the annealing rate between two filaments of respective lengths i and j, $F_{i,j}$ is the rate at which a filament of length $i+j$ fragments into two filaments of respective lengths i and j, and diffuse away (Fig. 1C). We note that events in which a filament is broken, but the fragments re-anneal before diffusing away, are not counted as fragmentation in this description (see Discussion). The dependence of these two rates on i and j encapsulates the key physical assumptions of our model. In a first version, we considered freely diffusing rigid filaments that associate end-to-end, yielding

$$K_{i,j} = \frac{K_{1,1}}{2}(i^{-1} + j^{-1}) \propto b\,(D_i + D_j)\,. \qquad (2)$$

Here, $K_{1,1}$ denotes the annealing rate for two isolated ULFs, and b is the ULF size. In general, $K_{1,1}$ depends on temperature, on the viscosity of the buffer and on the size of the ULFs. We assumed the filaments obey Rouse dynamics, *i.e.*, a simple model of free diffusion in the presence of a viscous friction against the surrounding fluid (38). This yields a diffusion coefficient $D_i \propto i^{-1}$ for a filament of length i (38). This set of assumptions implies that, in the absence of fragmentation, the

mean filament length $\langle L(t)\rangle$ increases as $t^{1/2}$ (39), consistent with our experimental data at short times, where fragmentation is negligible. It also gives a good description of the end-to-end annealing of actin (40). In a passive system (*e.g.*, in the absence of ATP hydrolysis), $F_{i,j}$ is connected to $K_{i,j}$ by the detailed balance requirement (37)

$$F_{i,j} = \frac{c_b\, e^{\epsilon_b/k_B T}}{2} K_{i,j} = \frac{K_d}{2} K_{i,j}\,, \qquad (3)$$

where c_b is a constant with the dimension of a concentration, $\epsilon_b < 0$ is the energy change associated to the formation of a bond, k_B the Boltzmann constant and T the absolute temperature. In the second equality, K_d is the equilibrium dissociation constant. The mean length at equilibrium, $\langle L_\infty\rangle$, only depends on K_d and total concentration and not on the specific form of $K_{i,j}$ (37). We solved Equation (1) numerically using Direct Simulation Monte Carlo (41). We fitted the theoretical predictions to the experimental data by using two free parameters: the dissociation constant K_d and the mean bond breaking time (bond lifetime) $\tau = F_{1,1}^{-1}$ (Fig. 1B, dashed lines). For low concentrations (c = 0.01, 0.03 and 0.1 mg.mL^{-1}), the model is in good agreement with the experimental data. A common fit over the three lowest densities, averaged over the three experimental repeats, yields a dissociation constant K_d = (1.00 ± 0.05) ×10^{-5} mg.mL^{-1} (mean ± SD, N = 3 repeats) equivalent to 6.1 ± 0.3 pM, and a mean bond breaking time $\tau = {F_{1,1}}^{-1} \simeq$13 ± 5 h. The resulting ULF annealing rate is $K_{1,1} = 2F_{1,1}/K_d =$ (7 ± 3) ×10^6 M^{-1}s^{-1}. We also attempted to fit the experimental data by setting $K_d = 0$ (no fragmentation), finding a worse quantitative agreement, *i.e.*, a larger sum of square residuals (Fig. S4 and Supplementary text).

Filament trapping by entanglement accounts for arrested assembly at high concentrations. At higher concentrations (c = 0.3 and 1.0 mg.mL^{-1}), the filament lengths predicted by the model were consistently longer than those observed in the experiments. This led us to speculate that our assumptions of freely diffusing filaments break down at such high concentrations, and that filaments become increasingly entangled as they grow longer. This would lead to a kinetically arrested state, where steric interactions between the filaments prevent them from annealing. One of us has previously shown that the resulting slowdown in association rates due to kinetic trapping is well described by a simple analytical approximation (42). To test our hypothesis, we modified our model to incorporate this mean-field kinetic trapping term in addition to fragmentation. The rationale of the model is that two filaments that come into contact at a finite angle must align in order to achieve their annealing. The annealing is prevented if the ambient concentration of filaments is so high that other filaments stand in the way of this alignment. Introducing γ as the largest angle allowing filament annealing in the absence of entanglement, we obtained

$$K^{\mathrm{ent}}{}_{i,j} = \frac{K_{1,1}}{2}(i^{-1} + j^{-1})\, g\left(\frac{c b^3 l^2{}_{\min}}{2}, \gamma\right) \qquad (4)$$

where $c = \sum_{k=1}^{\infty} k c_k$ is the total ULF concentration $l_{\min} = \min(i,j)$. Here, the function $g(x,\gamma) = \frac{1-[cos(\gamma)+xsin(\gamma)]e^{-\gamma x}}{(1+x^2)(1-cos(\gamma))}$ smoothly interpolates between 1 and 0 as x increases from 0 to ∞. This leads to an annealing rate identical to the one of Equation (2) for low c and $l_{\min}$, and accounts for the

slow-down of inter-filament reactions when these quantities are large. The fragmentation rate is still given by Equation (3), with $K_{i,j}$ replaced by $K^{\mathrm{ent}}{}_{i,j}$, as is appropriate in the absence of ATP hydrolysis. We moreover kept the previously estimated value K_d = 1.0 ×10^{-5} mg.mL^{-1}, as kinetic trapping should not affect the equilibrium properties of the system. Fitting the experimental data, we found γ= (7 ± 2) ×10^{-6} rad. This small value for the angle γ suggests that filaments must be locally perfectly aligned in order for annealing to occur. As shown by the solid curves in Figure 1B, this improved model yields a significantly better agreement with the experimental data. A common fit over the 5 concentrations (c = 0.01, 0.03, 0.10, 0.30 and 1.00 mg.mL^{-1}) averaged over the three experimental repeats, yields a mean bond lifetime τ = 18 ± 4 h (mean ± SD, N = 3) for this model. Note that entanglement has little impact on assembly dynamics at low concentrations, indicating that entanglement alone cannot explain the length saturation with time in these conditions (Fig. S4 and Supplementary text).

The filament length distribution supports kinetic trapping at high concentrations. The two mechanisms for the saturation of the filament lengths imply differences in the filament lengths distribution in the long-time, plateau regime. At low concentration, the system reaches thermodynamic equilibrium. Assuming that the bonding free energy of two filaments does not depend on their lengths, this implies that the filament lengths are exponentially distributed (37). At high concentration, small, highly mobile filaments react quickly, but the mobility and annealing rate of intermediate-length filaments is hindered by the surrounding tangle of other filaments. This situation implies a non-monotonic distribution of filament lengths, whereby short filaments are depleted while intermediate-length filaments accumulate due to their inability to react to form even longer filaments. To confirm this prediction, we investigated the distributions of filament length in the plateau regime (at t = 24 h) at low and high concentrations (Fig. 2A-B and S5). Our observations show a good agreement with our model in both regimes, with the low concentration distribution being purely exponential and the high concentration one showing a maximum, and thus confirm the existence of two distinct regimes for filament length saturation.

Vimentin IF assembly is reversible. The notion that filament length reaches an equilibrium at low concentrations implies that filament assembly should be balanced by disassembly. To clearly demonstrate that disassembly takes place, we shifted the equilibrium in the direction of filament shortening by diluting pre-assembled filaments. We diluted pre-assembled filaments at different dilution ratios and further incubated them at 37 °C for 6 h (Fig. 3A). We started from two different populations of filaments with a similar mean length of ~3 µm, obtained either (i) after 2 hours of growth with an initial concentration c_0 of 0.2 mg.mL^{-1} where filament entanglement has limited effects on assembly or (ii) after 0.5 h of growth with a c_0 of 1 mg.mL^{-1}, when filament entanglement plays a role (Fig. S6). Filaments shortened noticeably at low dilution ratio (1:10) and the shortening was even more pronounced at higher dilution ratio (1:100) in both conditions (Fig. 3B). After an extremely high dilution (1:1000), filaments appeared as single dots in fluorescence images, indicating massive disassembly. Length quantification showed a gradual decrease of the vimentin IFs length over time following dilution. Higher dilution ratios furthermore resulted in shorter filaments

(Fig. 3C). These results demonstrate the reversibility of vimentin IF assembly both under conditions that lead to equilibrium and to the kinetically arrested state.

Fragmentation and end-to-end annealing of vimentin IFs occur concomitantly. To obtain direct, filament-level evidence of the mechanisms at play during filament assembly, we performed dual color experiments that allowed us to follow the fate of segments of filaments as previously done in cells (14, 19). We mixed two pre-assembled (3 h at 37 °C) populations of vimentin filaments that were fluorescently labeled in different colors (green and red) and incubated them for another 6 h at 37 °C (Fig. 4A). Consistent with the observations of Fig. 1, we observed an increase of filament total length over time resulting from the annealing of filaments of different colors (Fig. 4B-C). We furthermore compared the length of single-color segments with the full length of the entire filaments and found that the mean length of the full filaments increased over time, the one of single-color segments decreased over time (Fig. 4C). These results show that vimentin filaments continuously fragment into shorter pieces while concomitantly re-annealing.

Discussion

In this paper, we show that the vimentin filament assembly is a reversible process. We started by observing that the mean length of vimentin IFs saturated after 24h of assembly. There could be several explanations for the filament length reaching a plateau: (i) the filaments become too long to diffuse and anneal over measurable time scales, (ii) the filament networks become too entangled, preventing annealing, or (iii) the filaments disassemble, either by depolymerization from the extremities or by fragmentation, which would compensate the effect of annealing at long times. We tested these different mechanisms by theoretical modeling and accumulated experimental evidence to show that the only way to fully explain the experimental data is to take into account the disassembly by fragmentation. The reduction of the assembly rate due to the slower diffusion of long filaments, which is included in our model, was not sufficient to explain the length plateau without the inclusion of fragmentation (Fig. S4). Similarly, the effect of entanglement was found to be important at high concentration (> 0.1 $mg.mL^{-1}$), but could not explain the plateau on its own without fragmentation, especially at low concentration (Fig. S4). Finally, the effect of depolymerization from filament extremities would decrease over time as the number of extremities decrease as a result of filament annealing, which was not compatible with the slowdown of assembly kinetics and the length saturation observed in the experimental data at long times.

While the long time scales necessary to observe the impact of fragmentation are similar to those observed for vimentin fragmentation and annealing in cells (14), they are 6 times longer than the time scales explored in previous *in vitro* studies with comparable conditions (concentrations, buffer, assembly at 37 °C), which may account for the dearth of previous characterization of vimentin fragmentation (27, 33, 35). Vimentin assembly has previously been probed over long time-scales (> 144 h) in a study of the link between filament length and mechanical properties of the network. However, these experiments were carried out at room temperature, which strongly slows down the

assembly dynamics and may have prevented the filaments from reaching an equilibrium over the experimental time scales (43).

Our characterization of vimentin length saturation is reminiscent of observations on microtubules (44) and F-actin (45), although the lengths of the latter two reach a plateau more quickly (< 1 h) in comparable conditions of protein concentration, salinity and temperature. In addition, the mechanisms involved there are different and fundamentally active: dynamical instability in the case of microtubules and filament treadmilling in the case of F-actin, although annealing and fragmentation also play a non-negligible role for microtubules and actin as well (45). Previous studies have also shown that entanglements could induce kinetic arrest in dense actin networks in the presence of actin crosslinkers (36, 42). In these studies, entanglements were shown to hinder the bundling of actin filaments. This bundling proceeds through a large-scale motion of filaments that become increasingly difficult in a dense network. The assembly of individual actin filaments was however largely unaffected by entanglement, due to the fact that it largely proceeds through the addition of single monomers, which can diffuse even in dense networks. By contrast, long vimentin filaments form through the annealing of shorter filaments, the diffusion of which can be severely hindered by entanglement. In cells, the concentration of intracellular vimentin has been estimated to be > 1 $mg.mL^{-1}$ (46) and most of the proteins are assembled into filaments except a small fraction of soluble tetramers (47). This suggests that filament entanglement might have an impact on vimentin assembly in the cytoplasm. However, it may be overcome by other processes, such as active transport. Unfortunately, the high density of intracellular vimentin networks, the difficulty to follow filament tips in cells and resolution limitations of live microscopy make the quantification of filament length over time extremely challenging. Technological advances are therefore still needed to investigate the regulation of vimentin filament length in cells.

The spontaneous fragmentation of vimentin filaments may appear at odds with their well-characterized mechanical resilience, which allows them to undergo stretching by up to 300 % without breaking (48–52). This apparent contradiction can however be resolved by noting the very different time scales involved in experiments where these behaviors are observed. Fragmentation is observed over several hours, while the mechanical properties of vimentin are typically probed over a few minutes at room temperature (48–52). While the molecular mechanism responsible for vimentin longitudinal stretching has been shown to involve the unfolding of vimentin subunits (51, 53, 54), the molecular mechanisms responsible for filament fragmentation need to be characterized in more detail. One possible hypothesis builds on the observation that vimentin filaments can exchange subunits along their length during filament assembly (30), implying that subunits can spontaneously dissociate from the filament structure and re-associate with other binding sites. We speculate that these association/dissociation events could randomly result in the appearance of weak spots along the filaments, which could be responsible for filament fragmentation. Filament fragmentation may occur only if a large enough number of subunits are missing locally, which could account for its low rate of occurrence (timescale of tens of hours) if we take into account the fact that the subunit exchange rate is already very slow, i.e. ~1% exchange per hour (30). This mechanism of fragmentation would also corroborate a previous report of vimentin filament polymorphism (55). Measurements of the lifetime of tetramers within filaments could help validate this hypothesis at the molecular level. Moreover, since the phosphorylation of vimentin has been shown to regulate vimentin assembly by modifying the exchange rate of subunits towards a high

off-rate in cells (56), it would be interesting to probe the impact of post-translational-modifications on the fragmentation mechanism. The softening of vimentin filaments observed after phosphorylation (57) may be associated with a high fragmentation rate.

The vimentin assembly dynamics observed in our experiments is well described by a mean-field model based on the Smoluchowski equation, which is based on the assumption that positions and orientations of the filaments are fully randomized within the network. In the model, the annealing rate of two filaments decreases when their lengths increase. This reflects the slower diffusion of long filaments compared to short ones, due to their larger friction with the surrounding fluid (see Equation (2)). Based on this assumption and the detailed balance condition of Equation (3), the total fragmentation rate $\sum F_{i,k-i}$ of a filament of length k does not increase linearly with k, as would be intuitively expected if all bonds broke independently and with the same rate. Instead, it increases much more slowly, specifically as $\ln(k)$, for long filaments. This behavior is however not incompatible with the aforementioned intuition. To understand this, we must note that the Smoluchowski formalism does not record microscopic bond-breaking events, but instead the instances where a bond breaks, then the resulting two filaments diffuse away from each other "to infinity", *i.e.*, by a length equal to several times their individual sizes. These latter instances are much rarer than the former in long, slowly-diffusing filaments. Indeed, most bond breaking events are followed by a re-binding event, rendered very likely by the resulting proximity of the filament ends. Likewise, the detailed balance condition (Eq. 2) imposes that the kinetic slow-down factor $g(cb^3{l^2}_{\min}/2, \gamma)$ introduced in Equation (4) applies equally to the fragmentation rate. Indeed, any physical process that hinders annealing must equally hinder the separation of the filaments following a bond breaking event, which increases the probability of their rapid re-binding. The success of this coarse mean-field approach to entanglements (Fig. 1B) suggests that the orientations of the filaments within the network remain largely random and isotropic throughout their assembly dynamics.

The annealing rate $K_{i,j}$ used in our model is distinct from that of the Hill model (58), which is often used in the literature (27, 31–33) and posits $K_{i,j} = [(\ln(i) + 0.312)/i + (\ln(j) + 0.312)/j]/(i + j)$ for rigid polymers undergoing end-to-end annealing. In particular, the Hill model predicts a slower filament growth than ours. To the best of our knowledge, none of the works that have made use of the Hill model to study the growth kinetics of vimentin have included fragmentation effects (27, 31–33). We compared our model to a version of Hill's *with fragmentation* in the Supplementary text and found that ours results in a better fit of the experimental data, especially in the early times. This could be related to the implicit assumption in the Hill model that rotational and translational diffusion are decoupled. The Hill model *without* fragmentation displays an even worse agreement with the experimental data (see Fig. S4).

Overall, our study provides new evidence that vimentin filaments can fragment spontaneously, making the assembly process reversible. In the future, it would be of interest to provide a molecular understanding of filament breakage and probe how it can be regulated by post-translational modifications, which are known to impact filament disassembly. Moreover, the existence of fragmentation could be also tested in other types of IFs such as desmin or keratin to see to what extent it is a general feature. Finally, since more than 90 diseases have been associated with mutations of IF proteins and most impact the assembly process, it would be also interesting to

probe specifically the effect of these mutations on the fragmentation rates. Overall, our results pave the way to new studies aiming at understanding the regulation of IF length, which plays a crucial role in IF dynamics and its related cellular functions.

Material and Methods

Detailed information about the experimental procedures are found in the Supplementary text. Briefly, we purified wild-type vimentin proteins from *E. coli* bacteria in denaturing conditions with 8M urea (59), then fluorescently labeled them through their single cysteine (29). For assembly experiments, vimentin was renaturated by stepwise dialysis in a sodium phosphate buffer (2.5 mM, pH 7.0). We used different concentrations of vimentin with a labeling rate of 20 %. We triggered the assembly by adding KCl (final concentration 100 mM) and incubated the solution at 37 °C. Furthermore, we took samples from the assembly solutions at different time points and fixed them with an equal volume of glutaraldehyde 0.5 % before imaging. For dilution experiments, we diluted pre-assembled filaments (at initial concentration 0.2 $mg.mL^{-1}$ for 2 h or 1.0 $mg.mL^{-1}$ for 30 minutes) with different ratios, from 1:10 to 1:1000, in the assembly buffer (sodium phosphate buffer 2.5 mM, pH 7.0, 100 mM KCl). The diluted filaments were incubated for another 6 h at 37 °C. For dual color experiments, we mixed equal volumes of two populations of pre-assembled filaments (both with an initial concentration of 0.2 $mg.mL^{-1}$ assembled for 3 h) labeled in two different colors, then incubated the mixture for another 6 h at 37 °C. We quantified the filament length manually using Fiji, and only filaments above 0.5 µm length were considered for analysis in the experiments with fluorescence microscopy. This has only a small impact on the comparison with the theory, see Fig. S7).

Acknowledgments

We thank Antoine Jégou, Stéphanie Portet, Guillaume Romet-Lemonne, Emmanuel Trizac, Raphaël Voituriez and Hugo Wioland for fruitful discussions. Cécile Leduc thanks Harald Herrmann and his group for teaching her the techniques involved in vimentin purification, and the support of the EU-supported Cooperation in Science and Technology (COST) action NANONET – Nanomechanics of intermediate filament networks. This project was funded by ANR-16-CE13-0019 (CL) and ANR-21-CE11-0004 (CL and ML), Marie Curie Integration Grant PCIG12-GA-2012-334053, “Investissements d’Avenir” LabEx PALM ANR-10-LABX-0039-PALM, ANR-15-CE13-0004-03, ERC Starting Grant 677532 (ML) and the 80|PRIME program of Centre National de la Recherche Scientifique (CL and ML). QDT and CL acknowledge the LabEx “Who am I?” (ANR-11-LABX-0071) and the Université Paris Cité IdEx (ANR-18-IDEX-0001) funded by the French Government through its ’Investments for the Future’ program."

References

1. E. Latorre, *et al.*, Active superelasticity in three-dimensional epithelia of controlled shape. *Nature* 563, 203–208 (2018).

2. J. Hu, *et al.*, High stretchability, strength, and toughness of living cells enabled by hyperelastic vimentin intermediate filaments. *Proc. Natl. Acad. Sci.* 116, 17175–17180 (2019).

3. R. Windoffer, A. Kölsch, S. Wöll, R. E. Leube, Focal adhesions are hotspots for keratin filament precursor formation. *J. Cell Biol.* 173, 341–348 (2006).

4. J. Ivaska, H.-M. Pallari, J. Nevo, J. E. Eriksson, Novel functions of vimentin in cell adhesion, migration, and signaling. *Exp. Cell Res.* 313, 2050–2062 (2007).

5. S. Etienne-Manneville, Cytoplasmic Intermediate Filaments in Cell Biology. *Annu. Rev. Cell Dev. Biol.* 34, 1–28 (2018).

6. S. Duarte, *et al.*, Vimentin filaments interact with the actin cortex in mitosis allowing normal cell division. *Nat. Commun.* 10, 4200 (2019).

7. M. P. Serres, *et al.*, F-Actin Interactome Reveals Vimentin as a Key Regulator of Actin Organization and Cell Mechanics in Mitosis. *Dev. Cell* 52, 210-222.e7 (2020).

8. Z. Ostrowska-Podhorodecka, *et al.*, Vimentin tunes cell migration on collagen by controlling β1 integrin activation and clustering. *J. Cell Sci.* 134 (2021).

9. M. Swoger, *et al.*, Vimentin Intermediate Filaments Mediate Cell Morphology on Viscoelastic Substrates. *ACS Appl. Bio Mater.* (2022).

10. P. J. Hollenbeck, A. D. Bershadsky, O. Y. Pletjushkina, I. S. Tint, J. M. Vasiliev, Intermediate filament collapse is an ATP-dependent and actin-dependent process. *J. Cell Sci.* 92, 621–631 (1989).

11. F. K. Gyoeva, V. I. Gelfand, Coalignment of vimentin intermediate filaments with microtubules depends on kinesin. *Nature* 353, 445–448 (1991).

12. B. T. Helfand, A. Mikami, R. B. Vallee, R. D. Goldman, A requirement for cytoplasmic dynein and dynactin in intermediate filament network assembly and organization. *J. Cell Biol.* 157, 795–806 (2002).

13. S. Wöll, R. Windoffer, R. E. Leube, Dissection of keratin dynamics: different contributions of the actin and microtubule systems. *Eur. J. Cell Biol.* 84, 311–328 (2005).

14. C. Hookway, *et al.*, Microtubule-dependent transport and dynamics of vimentin intermediate filaments. *Mol. Biol. Cell* 26, 1675–1686 (2015).

15. C. Leduc, S. Etienne-Manneville, Regulation of microtubule-associated motors drives intermediate filament network polarization. *J. Cell Biol.* 216, 1689–1703 (2017).

16. A. Robert, *et al.*, Kinesin-dependent transport of keratin filaments: a unified mechanism for intermediate filament transport. *FASEB J.* 33, 388–399 (2019).

17. M. W. Klymkowsky, L. A. Maynell, C. Nislow, Cytokeratin phosphorylation, cytokeratin filament severing and the solubilization of the maternal mRNA Vg1. *J. Cell Biol.* 114, 787–797 (1991).

18. G. Çolakoğlu, A. Brown, Intermediate filaments exchange subunits along their length and elongate by end-to-end annealing. *J. Cell Biol.* 185, 769–777 (2009).

19. A. Uchida, G. Colakoglu, L. Wang, P. C. Monsma, A. Brown, Severing and end-to-end annealing of neurofilaments in neurons. *Proc. Natl. Acad. Sci.* 110, E2696–E2705 (2013).

20. A. Robert, C. Hookway, V. I. Gelfand, Intermediate filament dynamics: What we can see now and why it matters. *BioEssays* 38, 232–243 (2016).

21. R. Kalluri, R. A. Weinberg, The basics of epithelial-mesenchymal transition. *J. Clin. Invest.* 119, 1420–1428 (2009).

22. H. Herrmann, U. Aebi, Intermediate Filaments: Structure and Assembly. *Cold Spring Harb. Perspect. Biol.* 8, a018242 (2016).

23. N. T. Snider, M. B. Omary, Post-translational modifications of intermediate filament proteins: mechanisms and functions. *Nat. Rev. Mol. Cell Biol.* 15, 163–177 (2014).

24. H. Herrmann, U. Aebi, Intermediate filament assembly: fibrillogenesis is driven by decisive dimer-dimer interactions. *Curr. Opin. Struct. Biol.* 8, 177–185 (1998).

25. H. Herrmann, M. Häner, M. Brettel, N.-O. Ku, U. Aebi, Characterization of distinct early assembly units of different intermediate filament proteins. *J. Mol. Biol.* 286, 1403–1420 (1999).

26. N. Mücke, *et al.*, Assessing the Flexibility of Intermediate Filaments by Atomic Force Microscopy. *J. Mol. Biol.* 335, 1241–1250 (2004).

27. R. Kirmse, *et al.*, A Quantitative Kinetic Model for the in Vitro Assembly of Intermediate Filaments from Tetrameric Vimentin. *J. Biol. Chem.* 282, 18563–18572 (2007).

28. M. E. Brennich, *et al.*, Dynamics of intermediate filament assembly followed in micro-flow by small angle X-ray scattering. *Lab. Chip* 11, 708–716 (2011).

29. S. Winheim, *et al.*, Deconstructing the Late Phase of Vimentin Assembly by Total Internal Reflection Fluorescence Microscopy (TIRFM). *PLoS ONE* 6 (2011).

30. B. Nöding, H. Herrmann, S. Köster, Direct Observation of Subunit Exchange along Mature Vimentin Intermediate Filaments. *Biophys. J.* 107, 2923–2931 (2014).

31. C. G. Lopez, O. Saldanha, K. Huber, S. Köster, Lateral association and elongation of vimentin intermediate filament proteins: A time-resolved light-scattering study. *Proc. Natl. Acad. Sci.* 113, 11152–11157 (2016).

32. S. Portet, *et al.*, Vimentin Intermediate Filament Formation: In Vitro Measurement and Mathematical Modeling of the Filament Length Distribution during Assembly. *Langmuir* 25, 8817–8823 (2009).

33. S. Portet, Dynamics of in vitro intermediate filament length distributions. *J. Theor. Biol.* 332, 20–29 (2013).

34. N. Mücke, *et al.*, In Vitro Assembly Kinetics of Cytoplasmic Intermediate Filaments: A Correlative Monte Carlo Simulation Study. *PLoS ONE* 11, e0157451 (2016).

35. N. Mücke, T. Wocjan, M. Jacquier, H. Herrmann, S. Portet, A general mathematical model for the in vitro assembly dynamics of intermediate filament proteins. *Biophys. J.* (2022).

36. T. T. Falzone, M. Lenz, D. R. Kovar, M. L. Gardel, Assembly kinetics determine the architecture of α-actinin crosslinked F-actin networks. *Nat. Commun.* 3, 861 (2012).

37. P. G. J. van Dongen, M. H. Ernst, Kinetics of reversible polymerization. *J. Stat. Phys.* 37, 301–324 (1984).

38. M. Rubinstein, R. H. Colby, *Polymer Physics* (Oxford University Press, 2003).

39. P. G. J. van Dongen, M. H. Ernst, Dynamic Scaling in the Kinetics of Clustering. *Phys. Rev. Lett.* 54, 1396–1399 (1985).

40. E. Andrianantoandro, L. Blanchoin, D. Sept, J. A. McCammon, T. D. Pollard, Kinetic mechanism of end-to-end annealing of actin filaments. *J. Mol. Biol.* 312, 721–730 (2001).

41. A. L. Garcia, C. van den Broeck, M. Aertsens, R. Serneels, A Monte Carlo simulation of coagulation. *Phys. Stat. Mech. Its Appl.* 143, 535–546 (1987).

42. G. Foffano, N. Levernier, M. Lenz, The dynamics of filament assembly define cytoskeletal network morphology. *Nat. Commun.* 7, 13827 (2016).

43. A. V. Schepers, *et al.*, Multiscale mechanics and temporal evolution of vimentin intermediate filament networks. *Proc. Natl. Acad. Sci.* 118 (2021).

44. K. Farrell, M. Jordan, H. Miller, L. Wilson, Phase dynamics at microtubule ends: the coexistence of microtubule length changes and treadmilling. *J. Cell Biol.* 104, 1035–1046 (1987).

45. D. Sept, J. Xu, T. D. Pollard, J. Andrew McCammon, Annealing Accounts for the Length of Actin Filaments Formed by Spontaneous Polymerization. *Biophys. J.* 77, 2911–2919 (1999).

46. D. B. Bekker-Jensen, *et al.*, An Optimized Shotgun Strategy for the Rapid Generation of Comprehensive Human Proteomes. *Cell Syst.* 4, 587-599.e4 (2017).

47. P. Soellner, R. A. Quinlan, W. W. Franke, Identification of a distinct soluble subunit of an intermediate filament protein: tetrameric vimentin from living cells. *Proc. Natl. Acad. Sci.* 82, 7929–7933 (1985).

48. L. Kreplak, H. Bär, J. F. Leterrier, H. Herrmann, U. Aebi, Exploring the mechanical behavior of single intermediate filaments. *J. Mol. Biol.* 354, 569–577 (2005).

49. Z. Qin, L. Kreplak, M. J. Buehler, Hierarchical Structure Controls Nanomechanical Properties of Vimentin Intermediate Filaments. *PLOS ONE* 4, e7294 (2009).

50. J. Block, *et al.*, Nonlinear Loading-Rate-Dependent Force Response of Individual Vimentin Intermediate Filaments to Applied Strain. *Phys. Rev. Lett.* 118, 048101 (2017).

51. J. Block, *et al.*, Viscoelastic properties of vimentin originate from nonequilibrium conformational changes. *Sci. Adv.* (2018).

52. C. Lorenz, *et al.*, Lateral Subunit Coupling Determines Intermediate Filament Mechanics. *Phys. Rev. Lett.* 123, 188102 (2019).

53. J. Forsting, J. Kraxner, H. Witt, A. Janshoff, S. Köster, Vimentin Intermediate Filaments Undergo Irreversible Conformational Changes during Cyclic Loading. *Nano Lett.* 19, 7349–7356 (2019).

54. F. Nunes Vicente, *et al.*, Molecular organization and mechanics of single vimentin filaments revealed by super-resolution imaging. *Sci. Adv.* 8, eabm2696 (2022).

55. H. Herrmann, *et al.*, Structure and Assembly Properties of the Intermediate Filament Protein Vimentin: The Role of its Head, Rod and Tail Domains. *J. Mol. Biol.* 264, 933–953 (1996).

56. J. E. Eriksson, *et al.*, Specific in vivo phosphorylation sites determine the assembly dynamics of vimentin intermediate filaments. *J. Cell Sci.* 117, 919–932 (2004).

57. J. Kraxner, *et al.*, Post-translational modifications soften vimentin intermediate filaments. *Nanoscale* 13, 380–387 (2021).

58. T. L. Hill, Length dependence of rate constants for end-to-end association and dissociation of equilibrium linear aggregates. *Biophys. J.* 44, 285–288 (1983).

59. H. Herrmann, L. Kreplak, U. Aebi, Isolation, characterization, and in vitro assembly of intermediate filaments. *Methods Cell Biol.* 78, 3–24 (2004).

Figures and Tables

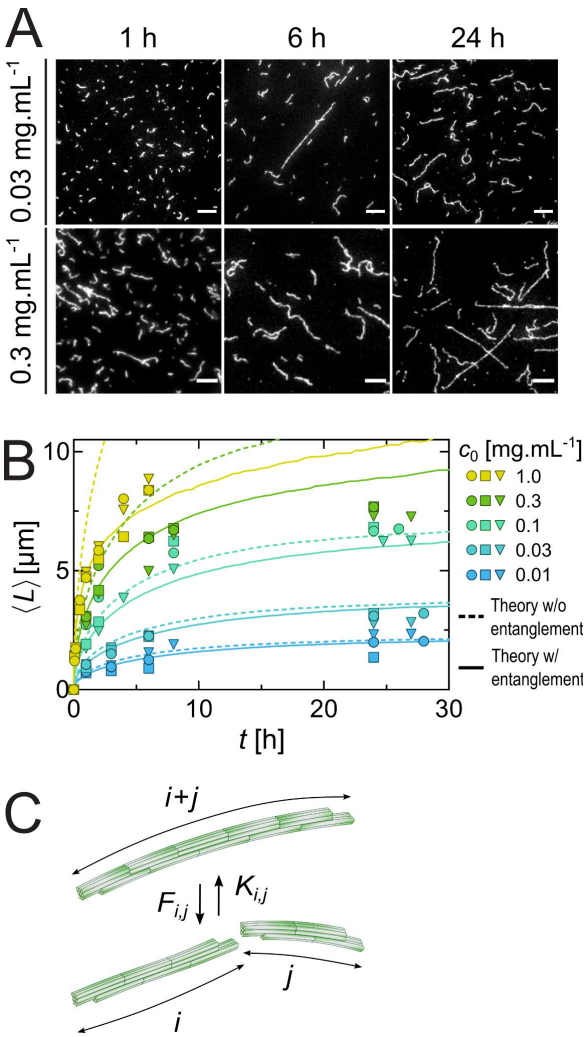

Figure 1. Filament length reaches a plateau during vimentin assembly. (A) Fluorescence images of *in vitro* vimentin filaments polymerized in assembly buffer at different initial concentrations, for a duration up to 28h at 37 °C. For 0.03 mg·mL^{-1}, filaments were fixed by mixing them with an equal volume of Glutaraldehyde 0.5%. For 0.3 mg·mL^{-1}, filaments were first diluted 20 times in assembly buffer before being fixed. Scale bar: 5 μm. (B) Evolution of the mean length $\langle L \rangle$ of vimentin filaments at different initial concentrations c_0 over time. Each data point was obtained from a sample size of ~200 filaments. The dashed lines correspond to theoretical fits from the model without entanglement, and the solid lines from the model with entanglement. Both fits were obtained via numerical simulations. (C) Schematics illustrating the annealing at rate $K_{i,j}$ and fragmentation at rate $F_{i,j}$ used in the theoretical model.

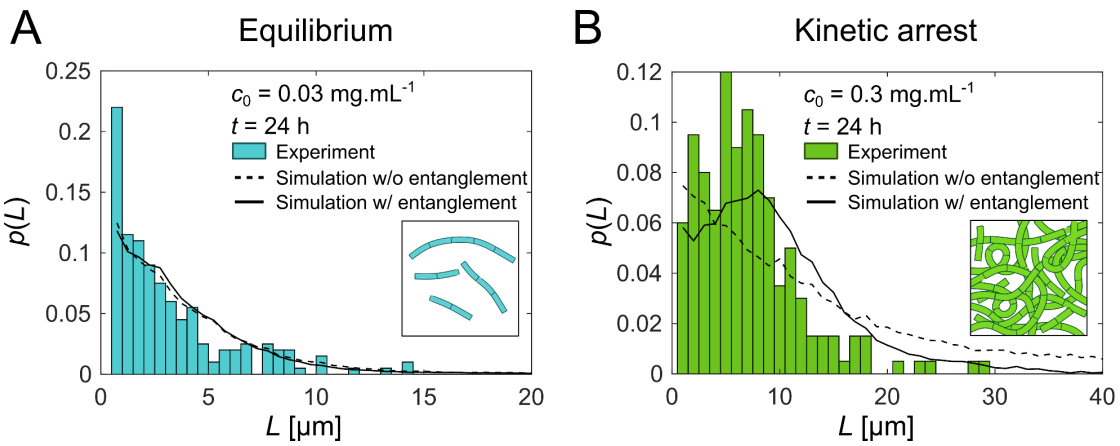

Figure 2. Length distributions after 24 h assembly. (A) Low concentration regime with initial concentration c_0 = 0.03 mg.mL^{-1} and assembly duration of 24 h; (B) high concentration regime with initial concentration c_0 = 0.3 mg.mL^{-1} and assembly duration of 24 h. The theoretical curves resulted from two simulation models. Dashed lines show the fit when only considering annealing and fragmentation, which results in an equilibrium state. Solid lines show the fit with the addition of entanglement, resulting in kinetic trapping. Due to limitations in fluorescence imaging, the filaments with L < 0.5 μm are excluded from both experiments and theory. Sample size: ~200 filaments.

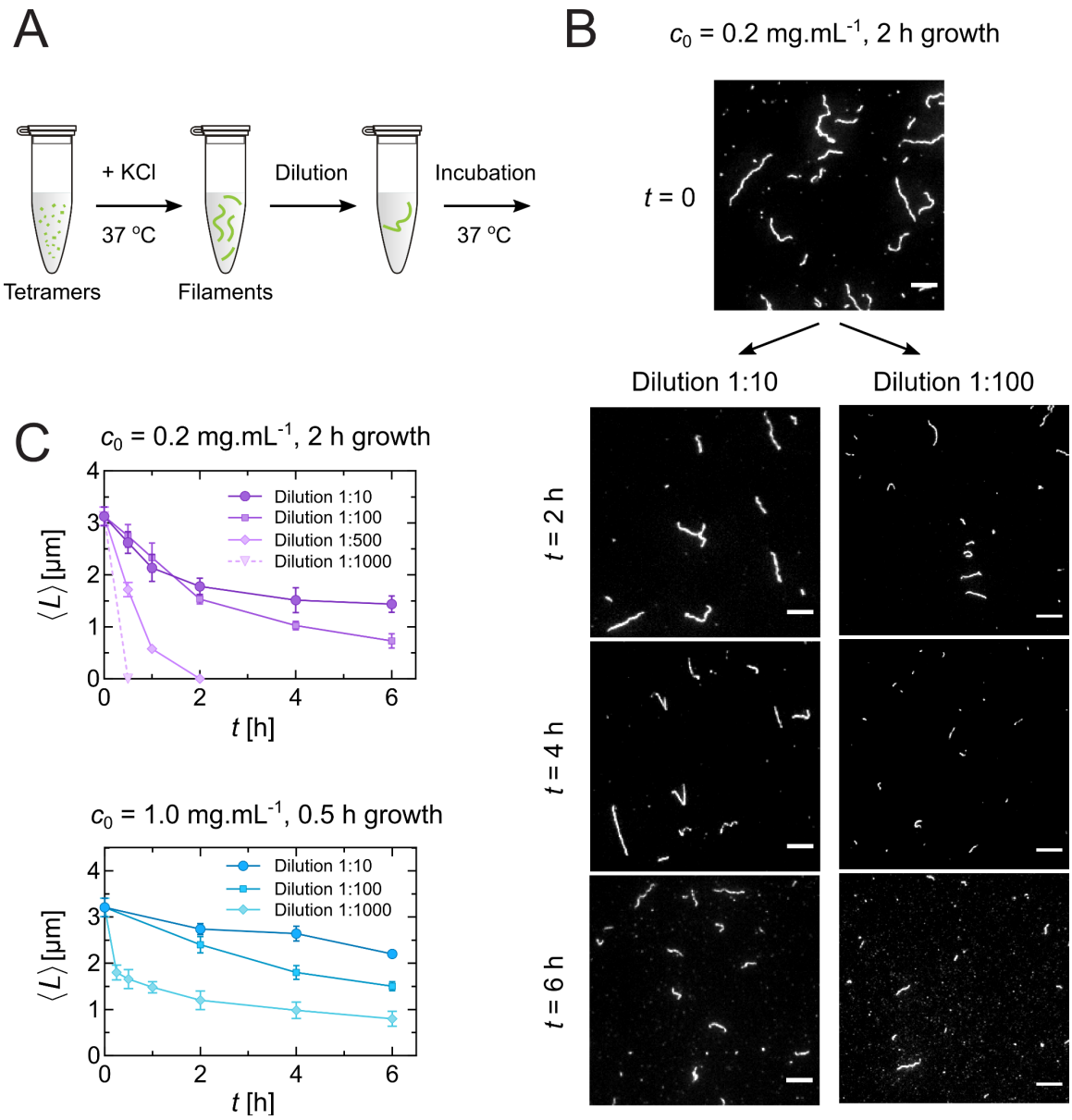

Figure 3. Vimentin assembly is reversible. (A) Schematics of the dilution experiment. Vimentin filaments are pre-assembled in the assembly buffer at 37°C. The obtained filaments are then diluted at different ratios from 1:10 to 1:1000, and further incubated at 37°C for up to 6 hours. (B) Fluorescence images of vimentin filaments, with initial concentration 0.2 mg.mL^{-1} and assembled for 2 h, at different time points after dilution. Scale bar: 5 μm. (C) Mean length of diluted filaments decreases over time. Error bars are standard deviations over 3 repeats. Sample size: ~200 filaments per condition and repeat.

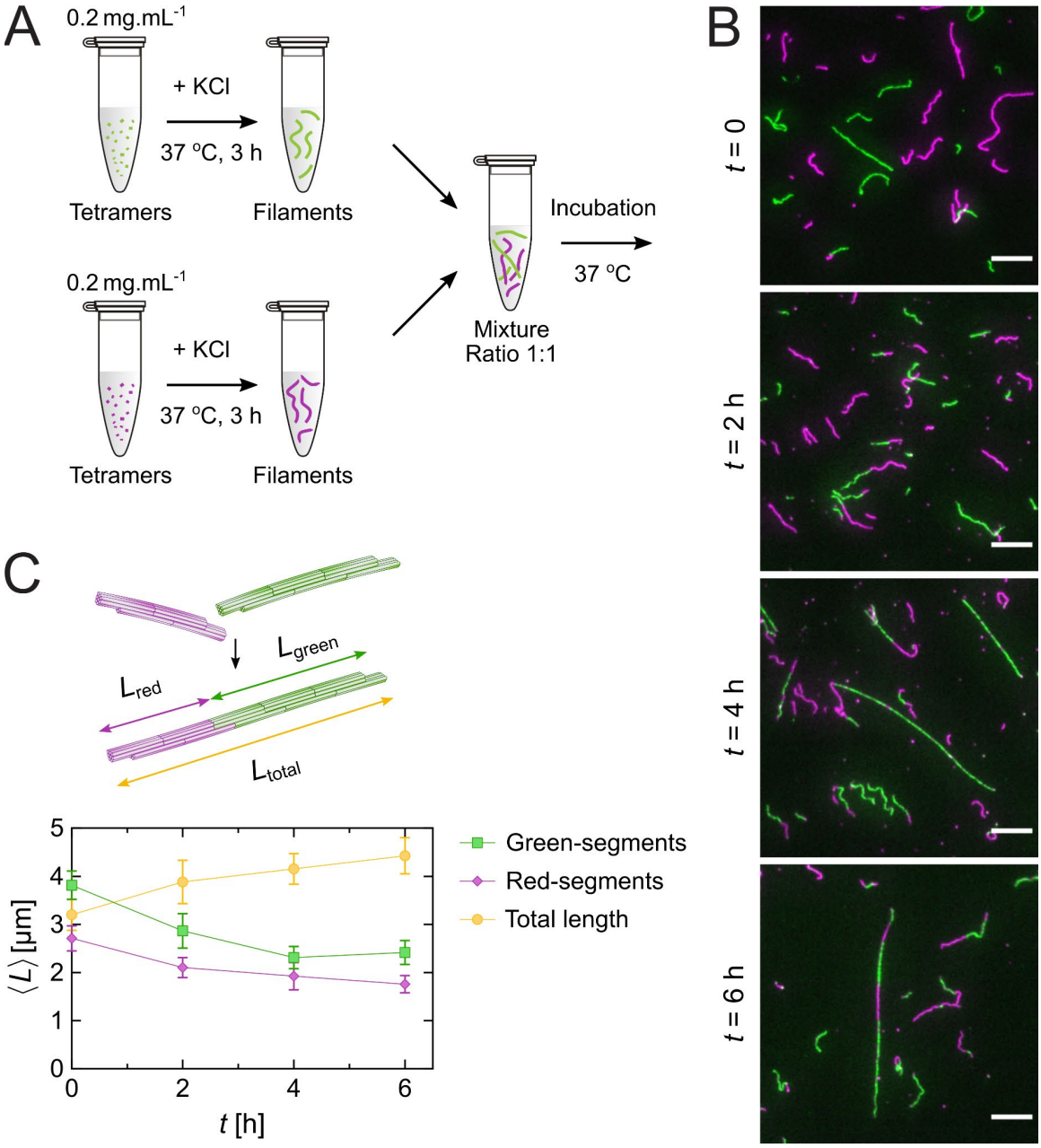

Figure 4. Annealing and fragmentation of vimentin filaments occur simultaneously during assembly. (A) Schematics of the dual color experiment. Two populations of vimentin filaments, both assembled from an initial concentration of 0.2 mg.mL^{-1}, labeled in green and red, were pre-assembled at 37°C for 3 h. Then, they were mixed together at ratio 1:1 and incubated for another 6 h. (B) Fluorescence images at different time points after mixing and incubation. Scale bar: 5 µm. (C) Mean total length of filaments (yellow), length of red (magenta) and green segments (green) over time after mixing and incubation. Error bars are standard deviations over 3 repeats. Sample size: ~200 filaments per condition and repeat.

Supplementary Information for

Vimentin intermediate filament assembly is a reversible process

Quang D. Tran, Valerio Sorichetti, Gerard Pehau-Arnaudet, Martin Lenz, and Cécile Leduc

Cécile Leduc and Martin Lenz.
E-mail: cecile.leduc@cnrs.fr and martin.lenz@universite-paris-saclay.fr

This PDF file includes:

Supplementary text
Figs. S1 to S11
Table S1
SI References

Supplementary figures

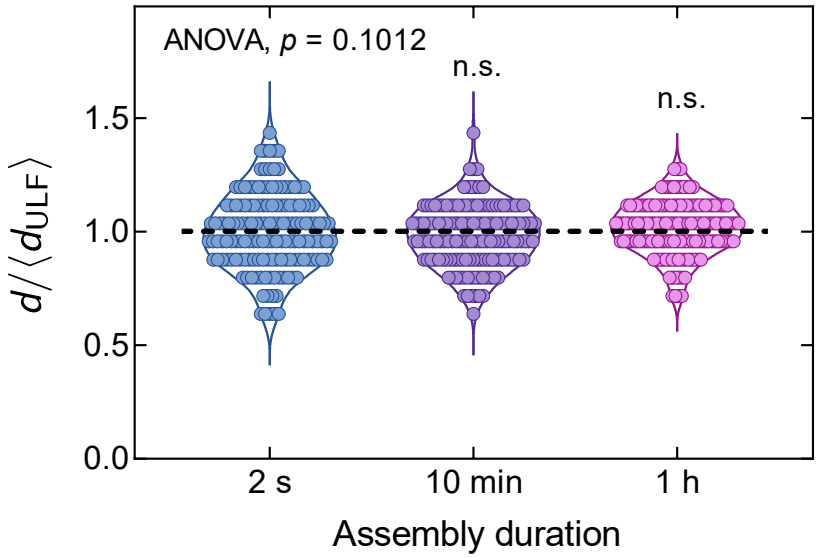

Fig. S1. Comparison of filament diameter at different assembly durations. Vimentin filaments were assembled at initial concentration of 0.1 $\mathrm{mg \cdot mL^{-1}}$ at 37 °C and samples were collected at different assembly durations (2 s, 10 minutes and 1 h). Filament diameter was measured from transmission electron microscopy images and normalized to the average diameter of ULFs obtained at 2 s assembly. Sample size: 150 filaments, one repeat.

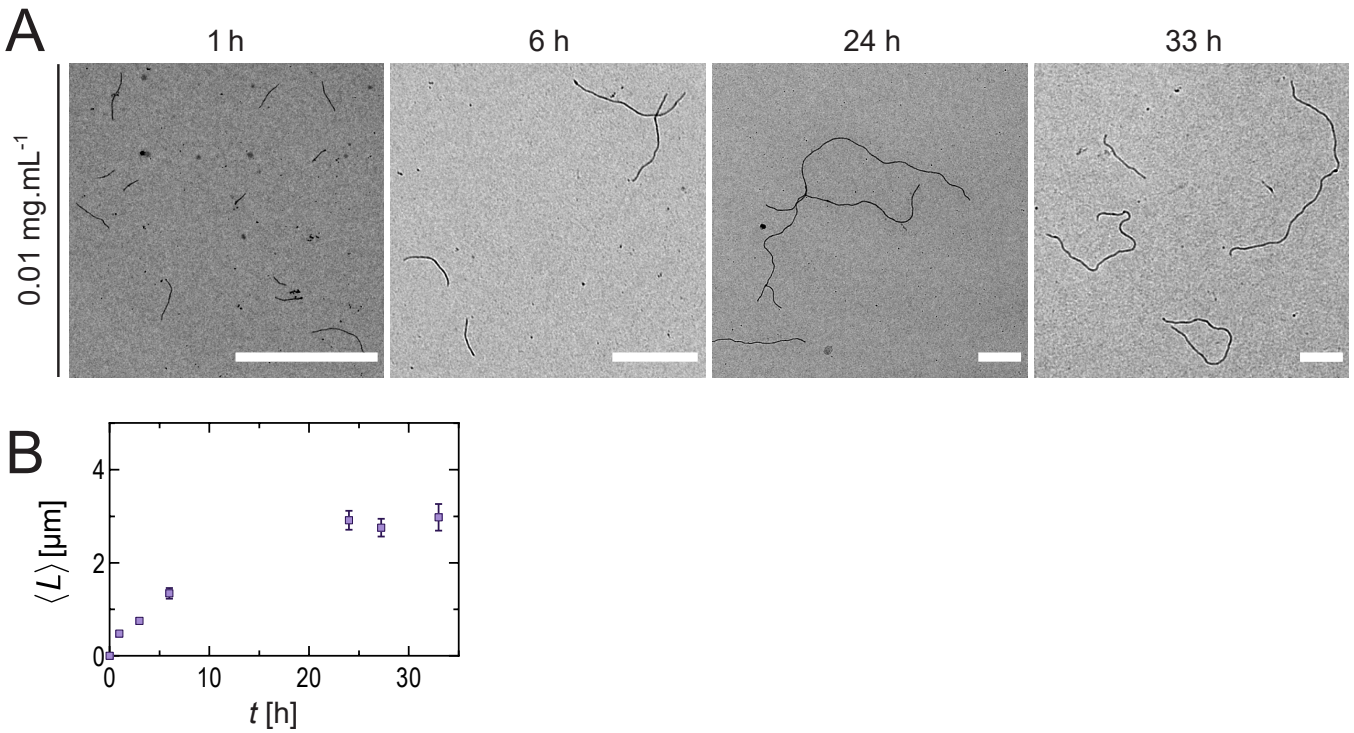

Fig. S2. Assembly of non-labeled vimentin filaments. **(A)** Transmission electron microscopy images of non-labeled vimentin filaments assembled at initial concentration of 0.01 $\mathrm{mg \cdot mL^{-1}}$, for duration of 33 h at 37 °C. Scale bar: 1 $\mu\mathrm{m}$. **(B)** Evolution of mean length of non-labeled vimentin filaments over time. Error bars are standard error, with sample size ∼150 filaments, one repeat.

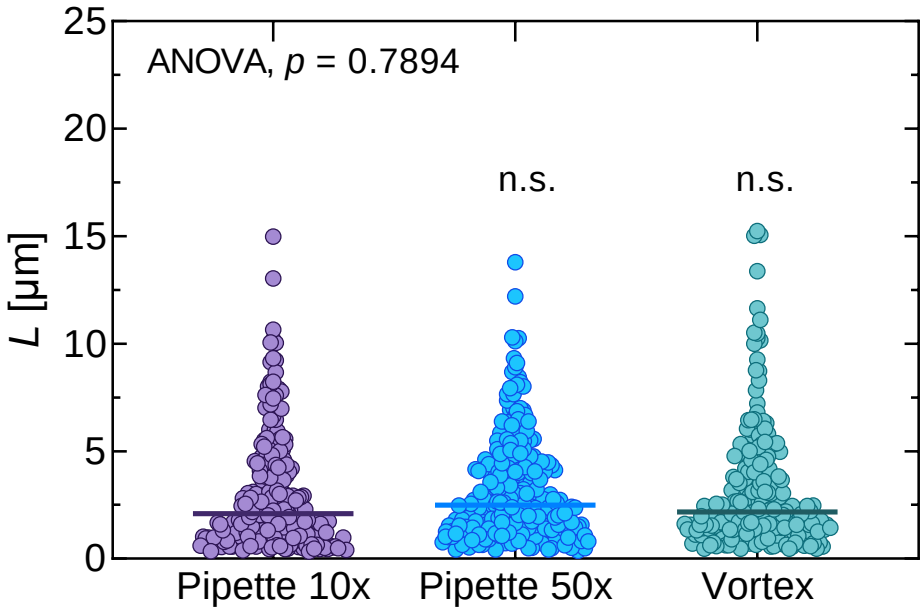

Fig. S3. Comparison between 3 methods of mixing filaments during sample preparation. Vimentin filaments were pre-assembled with initial concentration of 0.03 $\mathrm{mg \cdot mL^{-1}}$ for 28 h at 37 °C. Plain lines correspond to the median value. Filament length was measured from fluorescence images of filaments diluted from the same batch by 3 different mixing methods. Sample size: > 200 filaments, one repeat.

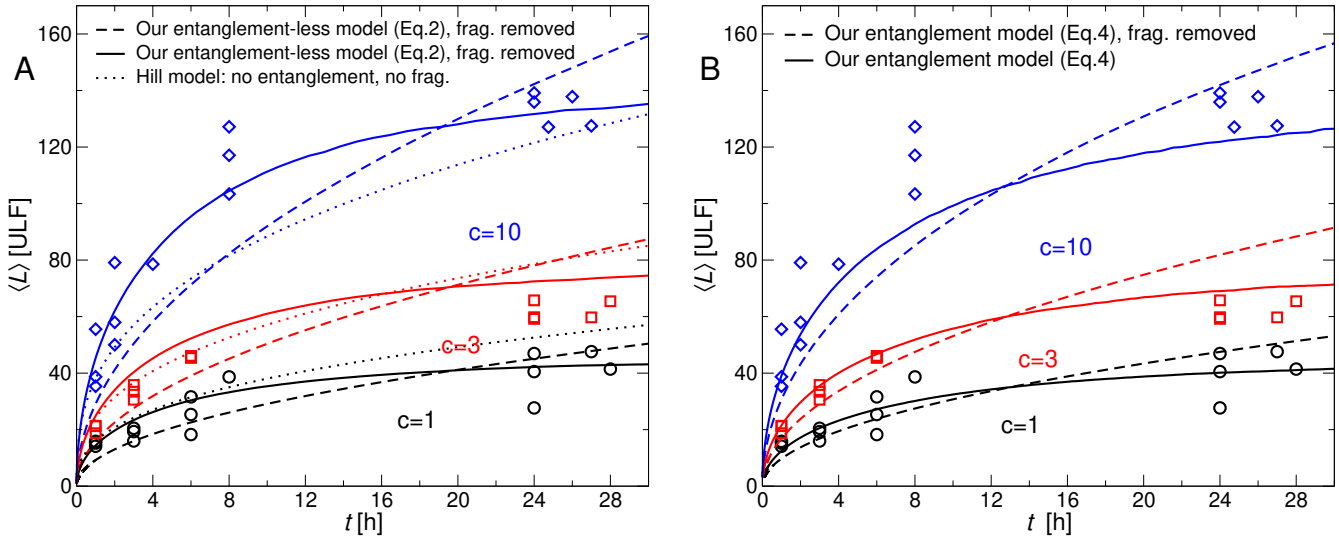

Fig. S4. Comparison of different models at low concentrations ($c = 1, 3, 10$ equivalent to 0.01, 0.03 and 0.1 mg.mL^{-1} in experiments). **(A)** Models *without entanglement*. Dashed lines: Our model, *i.e.*, $K_{i,j} = K_{1,1}(i^{-1} + j^{-1})/2$, without fragmentation ($K_d = 0$). Solid lines: Our model with fragmentation; $K_d = 1.0 \times 10^{-3}$, $\tau = 13$ h. Dotted lines: Hill model (Ref. 58 in the main text) without fragmentation ($K_d = 0$). **(B)** Models *with entanglement*. Dashed lines: model without fragmentation ($K_d = 0, \gamma = 7 \times 10^{-6}$). Solid lines: model with fragmentation ($K_d = 1.0 \times 10^{-3}, \gamma = 7 \times 10^{-6}$). The measured length (in μm) has been converted in ULFs using the following relation, which takes into account the ULF length of 49 nm after insertion in the filament, and 59 nm at the extremity (1): $\langle L_{\mathrm{ULF}} \rangle = 1 + (\langle L_{\mu\mathrm{m}} \rangle - 0.059)/0.049$.

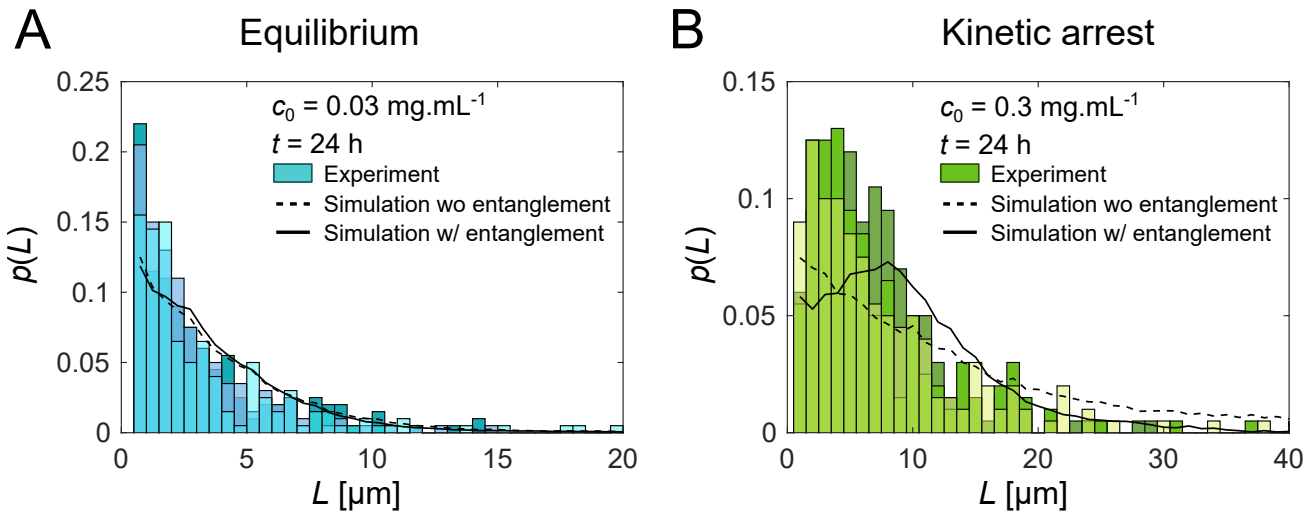

Fig. S5. Length distributions of vimentin filaments at the plateau regime at low and high concentrations, presented with 3 repeats (color brightness). **(A)** Low concentration regime with initial concentration $c_0 = 0.03\,\mathrm{mg}\cdot\mathrm{mL}^{-1}$ and assembly duration of 24 h; **(B)** high concentration regime with initial concentration $c_0 = 0.3\,\mathrm{mg}\cdot\mathrm{mL}^{-1}$ and assembly duration of 24 h. Sample size: ∼200 filaments per repeat. The theoretical curves resulted from two simulation models. Dashed lines show the fit when only considering annealing and fragmentation, which results in an equilibrium state. Solid lines show the fit with the addition of entanglement, resulting in kinetic trapping.

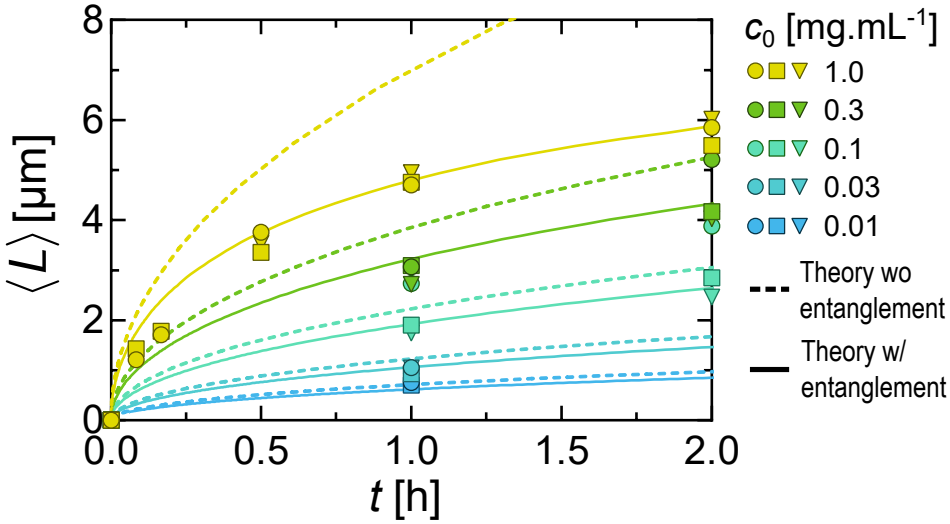

Fig. S6. Evolution of mean length $\langle L \rangle$ at early time of the assembly ($t \leq 2$ h) with different initial concentrations c_0. Each data point represents the average over $\sim$200 filaments. The dashed lines correspond to the theoretical fits from the model without entanglement, obtained via numerical simulations. The solid lines correspond to the theoretical model with entanglement. This figure is the same as Fig. 1B but with only the time from 0 to 2 h.

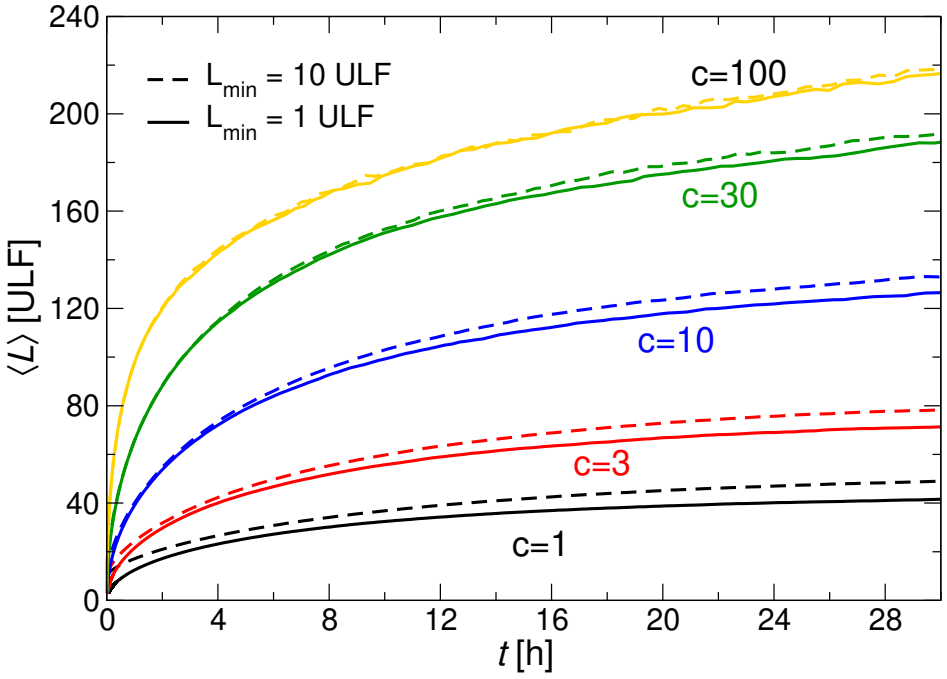

Fig. S7. Mean filament length from our simulation model, $K_{i,j} = K_{1,1}(i^{-1} + j^{-1})/2$, with fragmentation and with entanglement ($K_d = 1.0 \times 10^{-3}, \gamma = 7 \times 10^{-6}$). Dashed lines: mean length calculated considering only filaments with $L \geq 10$ ULF, corresponding to 0.5μm. Solid lines: data considering all filaments.

Supporting Information Text

Theoretical model and numerical simulations

A. Smoluchowski theory of annealing and fragmentation. In this Section, we introduce the Smoluchowski formalism to describe the annealing and fragmentation of vimentin filaments, and give more details on the interpretation of the Eqs. (1-3) reported in the main text. The Smoluchowski equation allows us to describe a system of objects –here polymeric filaments– which undergo aggregation and fragmentation reactions. Each filament is characterized by its length (or, equivalently, mass) k, measured in ULFs, and the number density of filaments of length k is denoted c_k. We assume that ULFs, *i.e.*, filaments of length $k = 1$, cannot break apart. The annealing rate between two filaments of lengths i and j is denoted $K_{i,j}$, whereas the fragmentation rate is denoted $F_{i,j}$.

We make three main assumptions (2): (i) No branching is allowed (each ULF can bind to two others at most), nor the formation of loops. (ii) The same free energy difference $\Delta f_b < 0$ is associated with the formation of any bond. (iii) Detailed balance is respected, so that at equilibrium the rate of losing k-mers to fragmentation into i- and j-mers is exactly compensated by the rate of gaining k-mers from the annealing of i- and j-mers. Mathematically, the condition (iii) is expressed as follows:

$$\frac{F_{i,j}}{K_{i,j}} = \frac{ce^{\Delta f_b/k_BT}}{2} = \frac{K_d}{2}, \tag{S1}$$

where k_B is Boltzmann's constant, T is the absolute temperature, and c is the total number density of ULFs. Here K_d is the equilibrium dissociation constant characterizing the reaction. We note that this quantity does not depend on the total ULF density c. To show this, we start by expressing K_d, from Eq. (S1), as

$$K_d = ce^{\Delta f_b/k_BT}, \tag{S2}$$

We can write this free energy change as the sum of an energetic term $\epsilon_b < 0$ and an entropic term $T\Delta s_b < 0$:

$$\Delta f_b = \epsilon_b - T\Delta s_b, \tag{S3}$$

with

$$\Delta s_b = k_B \ln\left(\frac{c}{c_b}\right), \tag{S4}$$

where $c_b \propto v_b^{-1}$, with v_b sometimes called the "bonding volume"(3). We thus conclude that

$$K_d = c_b e^{\epsilon_b/k_BT}. \tag{S5}$$

From the last expression, it is apparent that K_d only depends on the physics of the bonding process and on temperature, and not on the total density c.

Under the assumptions (i–iii) reported above, the concentrations $c_k(t)$ of filaments of length k are governed by the Smoluchowski equation (2):

$$\dot{c}_k = \frac{1}{2}\sum_{i=1}^{k-1}(K_{i,k-i}c_ic_{k-i} - F_{i,k-i}c_k) - \sum_{i=1}^{\infty}(K_{i,k}c_ic_k - F_{i,k}c_{i+k}), \tag{S6}$$

where all the c_k depend implicitly on time and we have additionally assumed that $K_{i,j} = K_{j,i}$ and $F_{i,j} = F_{j,i}$. Here we consider a reaction rate which is appropriate for freely diffusing rigid filaments which undergo Rouse dynamics and anneal end-to-end. For this system, we expect $K_{i,j} \propto b(D_i + D_j)$, where b is the ULF size and D_i is the Rouse diffusion coefficient, which scales as $D_i \propto i^{-1}$ (4). This amounts to applying the Smoluchowski formula, $K_{i,j} \propto (D_i + D_j)R_{i,j}$, with $R_{i,j}$ the target size (reaction radius) (5), to a target of size b diffusing with the diffusion coefficient of the whole filament. Thus, we have

$$K_{i,j} = \frac{K_{1,1}}{2}\left(i^{-1} + j^{-1}\right). \tag{S7}$$

The dynamics is additionally constrained by the requirement that no ULFs are created or destroyed, *i.e.*, the total mass of the system is conserved:

$$\sum_{k=1}^{\infty} kc_k = \frac{N}{V} = c, \tag{S8}$$

where N is the total number of ULFs and V is the system's volume.

Eq. (S6) implies that in a time interval Δt and in the volume V we will have:

$$K_{i,j}c_ic_j\left(1 - \frac{\delta_{i,j}}{2}\right)V\Delta t \quad \text{annealing events between an } i\text{-mer and a } j\text{-mer}, \tag{S9}$$

and

$$F_{i,j}c_{i+j}\left(1-\frac{\delta_{i,j}}{2}\right)V\Delta t \quad \text{fragmentation events producing an } i\text{-mer and a } j\text{-mer}, \tag{S10}$$

where $\delta_{i,j}$ is the Kronecker delta. The quantity in parentheses is introduced to avoid double-counting of reactions involving filaments of the same length ($i = j$). This is due to the fact that reactions with $i = j$ are twice as rare as those with $i \neq j$. This can be understood by considering, for example, a 4-mer and denoting the the probability per unit time that any of the three bonds in the 4-mer breaks as p_{break}. One can then easily see that the probability per unit time that the 4-mer breaks into a 1-mer and a 3-mer is $2p_{\text{break}}$, whereas the probability that it breaks into two 2-mers is p_{break}.

An important quantity we are interested in is the mean filament length at equilibrium, defined as

$$\langle L_\infty\rangle = \frac{\sum_k kc_k(\infty)}{\sum_k c_k(\infty)}. \tag{S11}$$

This quantity does not depend on the form of $K_{i,j}$ (and $F_{i,j}$), but only on the equilibrium constant K_d and on c, and it can be computed analytically. One finds (2):

$$\langle L_\infty\rangle = \frac{1+\sqrt{1+8(c/K_d)}}{2} \simeq \sqrt{\frac{2c}{K_d}}, \tag{S12}$$

where the approximation is valid for large c/K_d (weak fragmentation). We will see in what follows that for the experimental system studied in this work, this approximation is valid.

In what follows, we will use for simplicity dimensionless quantities, defined by rescaling times by $\tau = F_{11}^{-1}$ (the average breaking time of a bond between two ULFs) and all ULF densities by c_0, the lowest ULF number density used in the experiments (corresponding to a vimentin concentration of 0.01 mg/mL). This yields, denoting the dimensionless quantities by a tilde:

$$\tilde{K}_{i,j} = c_0\tau K_{i,j}, \qquad \tilde{F}_{i,j} = \tau F_{i,j}, \quad \text{and} \quad \tilde{K}_d = c_0 K_d. \tag{S13}$$

We note that with this choice of dimensionless quantities one has $\tilde{F}_{1,1} = 1$ and thus

$$\tilde{K}_{i,j} = \tilde{K}_d^{-1}(i^{-1}+j^{-1}) \quad \text{and} \quad \tilde{F}_{i,j} = \frac{1}{2}(i^{-1}+j^{-1}). \tag{S14}$$

In the following Sections, we will drop the tilde when referring to dimensionless quantities for clarity.

B. Description of the DSMC algorithm. Since the Smoluchowski equation Eq. (S6) can only be solved analytically for certain forms of $K_{i,j}$, we use here a numerical approach, called Direct Simulation Monte Carlo (DSMC) (6–8). DSMC is a powerful stochastic method to solve differential equations such as Eq. (S6), which samples the correct dynamics in the limit of large system sizes/large number of samples. We will here mainly follow the algorithm described in Ref. (6): The starting point is an array $\mathbf{m}$ of length N, each element α of which contains a number m_α which represents the length of filament α:

$$\mathbf{m} = (m_1, m_2, \ldots, m_N).$$

An element $m_\alpha = 0$ represents the absence of a filament; moreover, we have $\sum_{\alpha=1}^{N} m_\alpha = N$ (total number of ULFs) because of mass conservation. Here, we choose $N = 10^5$. To reflect the initial conditions in experiments, we additionally assume that the initial state of the system is

$$\mathbf{m}_0 = (1, 1, \ldots, 1),$$

i.e., only monomers are present.

After the array $\mathbf{m}$ is initialized, we run the DSMC simulation, which consists in repeating a large number of times a Monte Carlo step (described below). The execution is arrested when the simulation time exceeds the equivalent experimental time.

Description of the Monte Carlo step. In this paragraph, we will describe the single Monte Carlo (MC) step, which is repeated a large number of times during the numerical resolution of Eq. (S6) performed using the DSMC algorithm.

With reference to Eq. (S6), we define two quantities which will be useful in the description of the MC step below: $n \equiv V\sum_{i=1}^{\infty} c_i$ (total number of filaments) and $l \equiv V\sum_{i=2}^{\infty} c_i$ as (total number of filaments of length ≥ 2). We recall that only filaments of length 2 or more can undergo fragmentation.

Before the start of the simulation, we give an estimate of the maximum annealing rate $K_{\max}$ and of the maximum fragmentation rate $F_{\max}$. The exactness of the algorithm does not depend on this initial choice, however choosing values which are too far from the actual maximum rates can lead to a reduced efficiency (6). For the annealing rate, Eq. (S7), the maximum is by definition $K_{\max} = K_{1,1} = 2K_d^{-1}$ in dimensionless units. We thus have $F_{\max} = F_{1,1} = 1$ as an estimate for the maximum fragmentation rate.

During every MC step, we either attempt to perform an annealing reaction (with probability p) or a fragmentation one (with probability $1-p$). The value of p is calculated initially and then updated during the course of the simulation in such a way that the average number densities c_k satisfy Eq. (S6). At the beginning of each MC step, p is evaluated as

$$p^{-1} = 1 + \frac{lNF_{\max}}{n(n-1)cK_{\max}}. \quad [S15]$$

We will show below that this choice also guarantees that the simulation samples the correct number of fragmentation and annealing events per unit volume and unit time as are required by Eq. (S6).

We define a *waiting time* variable that is set to zero at the beginning of the simulation. After each reaction, a waiting time increment is generated: These increments are also chosen in order to guarantee the correct number of annealing and fragmentation reaction per unit time/volume, as detailed below.

We can now describe the MC step, during which the following actions are performed:

1. We evaluate the probability of annealing p according to Eq. (S15). The explicit form of p, Eq. (S15), will be discussed in detail below.

2. We pick a random number $0 \leq R \leq 1$ from a uniform distribution. If $R \leq p$, we attempt a coalescence event:

   (a) We pick a pair of elements of the array $\mathbf{m}$, denoted α, β at random. Since there are $n(n-1)$ ordered pairs of elements to choose from, the probability to pick a specific pair is $[n(n-1)]^{-1}$. Let the length associated with these elements be $m_\alpha = i$ and $m_\beta = j$.

   (b) We evaluate the annealing rate (in dimensionless units) as $K_{i,j} = K_d^{-1}(i^{-1} + j^{-1})$. If $K_{i,j} > K_{\max}$, we set $K_{\max} = K_{i,j}$ and return to (1). Otherwise, we continue.

   (c) We pick another random number $0 \leq R' \leq 1$ from a uniform distribution, and perform coalescence if $R' \leq K_{i,j}/K_{\max}$. If coalescence is unsuccessful, we return to (1). Otherwise, we continue.

   (d) We increment the waiting time by $\Delta t^a_{i,j} = \frac{2AN}{n(n-1)cK_{i,j}}$. Here A is a parameter, the only condition on which is that it must be between 0 and 1, as we will discuss in more detail below.

   (e) After updating the waiting time, we also update the array $\mathbf{m}$ by setting $m_\alpha = 0$ and $m_\beta = i + j$.

3. If $R > p$, we attempt to perform a fragmentation event:

   (a) We pick at random an element γ of the array $\mathbf{m}$, with the condition that its length m_γ is equal to or larger than 2. The probability of choosing a particular element under this condition is l^{-1}.

   (b) We pick the length i of the first of the two fragments in which the filament will be fragmented ($1 \leq i \leq k-1$) with probability $(m_\gamma - 1)^{-1}$. The length of the second fragment is then $k - i$.

   (c) We evaluate the fragmentation rate as $F_{i,k-i} = [i^{-1} + (k-i)^{-1}]/2$. If $(k-1)F_{i,k-i} > F_{\max}$, we set $F_{\max} = (k-1)F_{i,k-i}$ and return to (1). Otherwise, we continue.

   (d) We extract another random number $0 \leq R'' \leq 1$ from a uniform distribution, and perform fragmentation if $R'' \leq (k-1)F_{i,k-i}/F_{\max}$. If fragmentation is unsuccessful, we return to (1). Otherwise, we continue.

   (e) We increment the waiting time by $\Delta t^f_{i,k-i} = \frac{2(1-A)}{l(k-1)F_{i,k-i}}$, with A defined above in step (2). We will show below that choosing $1 - A$ here guarantees that the correct number of fragmentation events per unit time is obtained.

   (f) After updating the waiting time, we also update the array $\mathbf{m}$ by setting the length of an element at random which has length 0 to i and setting m_γ to $k - i$.

Below, we prove that the definition of p (Eq. (S15)) and the waiting time increments $\Delta t^a_{i,j}$ (for annealing) and $\Delta t^f_{i,k-i}$ (for fragmentation) give a number of annealing and fragmentation events per unit time which is consistent with the Smoluchowski equation, Eq. (S6).

Over a single MC step, the mean number of annealing events involving the pair (α, β) of elements of $\mathbf{m}$ with masses $m_\alpha = i, m_\beta = j$ is

$$\langle \#a_{\alpha,\beta} \rangle \equiv \frac{p}{n(n-1)} \frac{K_{m_\alpha, m_\beta}}{K_{max}}. \quad [S16]$$

We note that in the algorithm we consider (m_α, m_β) as an ordered pair, and thus in Eq. (S16) we consider the reaction $(i,j) \to k$ as distinct from $(j,i) \to k$. The mean number of annealing events involving *any two filaments* with lengths i, j can be obtained by multiplying the above quantity by $2(1 - \delta_{i,j}/2)V^2 c_i c_j$. The factor $2(1 - \delta_{i,j}/2)$ takes into account the fact that, as mentioned above, for $i \neq j$, there are two ways to perform the annealing, whereas for $i = j$ there is only one. The factor $V^2 c_i c_j$ is the product of the volume fractions of filaments of lengths i and j. We thus have

$$2V^2 c_i c_j \left(1 - \frac{\delta_{i,j}}{2}\right) \times \frac{p}{n(n-1)} \frac{K_{i,j}}{K_{max}} = K_{i,j} c_i c_j \left(1 - \frac{\delta_{i,j}}{2}\right) V \Delta t, \quad [S17]$$

where we have equated the mean number of annealing events involving any two filaments with lengths i, j to the value required by the Smoluchowski equation, Eq. (S9). From the equality Eq. (S17) we obtain, recalling that $c = N/V$,

$$\Delta t = \frac{2pN}{n(n-1)cK_{\max}}. \tag{S18}$$

Eq. (S18) relates the time interval Δt to the probability of annealing. We will now obtain a second equality involving p and Δt, which will allow us to prove that the expression Eq. (S15) for p guarantees the correct number of fragmentation and coagulation events per unit time.

When performing a fragmentation event of a filament γ with mass m_γ, we consider the two fragments of size $i, m_\gamma - i$ in which it breaks as an ordered pair and thus $m_\gamma \to (i, m_\gamma - i)$ is distinct from $m_\gamma \to (m_\gamma - i, i)$. The mean number of fragmentation events involving filament γ where the first fragment of the ordered pair has length i is thus

$$\langle \# f_{\gamma;i} \rangle \equiv \frac{(1-p)}{l(m_\gamma - 1)} \frac{(m_\gamma - 1)F_{i,m_\gamma - i}}{F_{\max}} = \frac{(1-p)}{l} \frac{F_{i,m_\gamma - i}}{F_{\max}}. \tag{S19}$$

To obtain the mean number of fragmentations of a generic $k-$mer where any one of the fragments has length i we need to multiply this quantity by $2(1-\delta_{i,k-i})Vc_k$, similarly to what we have done in the case of annealing:

$$2Vc_k \left(1 - \frac{\delta_{i,k-i}}{2}\right) \times \frac{(1-p)}{l} \frac{F_{i,k-i}}{F_{\max}} = F_{i,k-i} c_k \left(1 - \frac{\delta_{i,k-i}}{2}\right) V \Delta t. \tag{S20}$$

We have thus obtained a second equality involving Δt:

$$\Delta t = \frac{2(1-p)}{lF_{\max}}. \tag{S21}$$

By equating the two expressions for Δt, Eq. (S18) and Eq. (S21), we find Eq. (S15). We have thus proven that the latter is the correct expression of p, which gives the correct number of fragmentation and annealing events per unit time and unit volume, as required by the Smoluchowski equation.

Finally, we will prove that the constants A and $1-A$ introduced when calculating the waiting time increments are consistent with Eq. (S18) and Eq. (S21). To show this, it is sufficient to observe that the total time increment during a MC step is:

$$\begin{aligned}
\Delta t &= \sum_{0 \le \alpha < \beta \le n-1} \langle \# a_{\alpha,\beta} \rangle \Delta t^a_{m_\alpha, m_\beta} + \sum_{k=0}^{l-1} \sum_{i=1}^{m_\gamma - 1} \langle \# f_{\gamma;i} \rangle \Delta t^f_{i, m_\gamma - i} \\
&= \sum_{0 \le \alpha < \beta \le n-1} \left[\frac{pK_{m_\alpha, m_\beta}}{n(n-1)K_{\max}} \right] \left[\frac{2AN}{n(n-1)cK_{m_\alpha, m_\beta}} \right] \\
&\quad + \sum_{k=0}^{l-1} \sum_{i=1}^{m_\gamma - 1} \left[\frac{(1-p)F_{i,m_\gamma - i}}{lF_{\max}} \right] \left[\frac{2(1-A)}{l(m_\gamma - 1)F_{i,m_\gamma - i}} \right] \\
&= \frac{2ANp}{n(n-1)cK_{\max}} + \frac{2(1-A)(1-p)}{lF_{\max}}
\end{aligned} \tag{S22}$$

One can see that this equality is cnsistent with Eq. (S18) and Eq. (S21). We note that the algorithm samples on average the correct kinetics independently of the value of A, as long as $0 \le A \le 1$. Here we take $A = 1$, meaning that the waiting time increment is calculated only after a successful annealing reaction, but not after a successful fragmentation reaction. This choice reduces the statistical noise on the data at short and intermediate times, where fragmentation is negligible and the filaments mostly undergo annealing reactions.

C. Fitting the experimental data. In this Section, we describe the procedure followed to fit the experimental data shown in Fig. 1B of the main text (mean filament length L as a function of time) using the numerical results obtained with the DSMC simulations (Sec. B).

The objective of this fit is to determine the values of K_d (equilibrium dissociation constant) and τ (average bond breaking time) that best describe the experimental data. Since the data for $c > 10$ (corresponding to 0.1 mg/mL in experimental units) display the signature of a kinetic slowing down due to entanglement, as discussed in the main text, we have decided to fit only the data corresponding to the three lowest densities ($c = 1, 3$ and 10) to determine the values of K_d and τ. This is also justified *a posteriori* by comparing the fit results obtained by considering the three lowest, four lowest, or all the densities, as we discuss below.

We have run for each one of the densities $c = 1, 3, 10$ DSCM simulations for different values of the equilibrium dissociation constanst K_d. For each pair of (c, K_d) values, in order to improve the statistics we have performed 50 independent simulations, in each one of which the random number generator was initialized with a different seed. From each simulation, we have obtained the mean length as a function of time, $\langle L(t/\tau) \rangle$; we have then averaged the $\langle L(t/\tau) \rangle$ curves produced from these simulations to obtain a single theoretical curve $\langle L_{\text{sim}}(c, K_d; t/\tau) \rangle$.

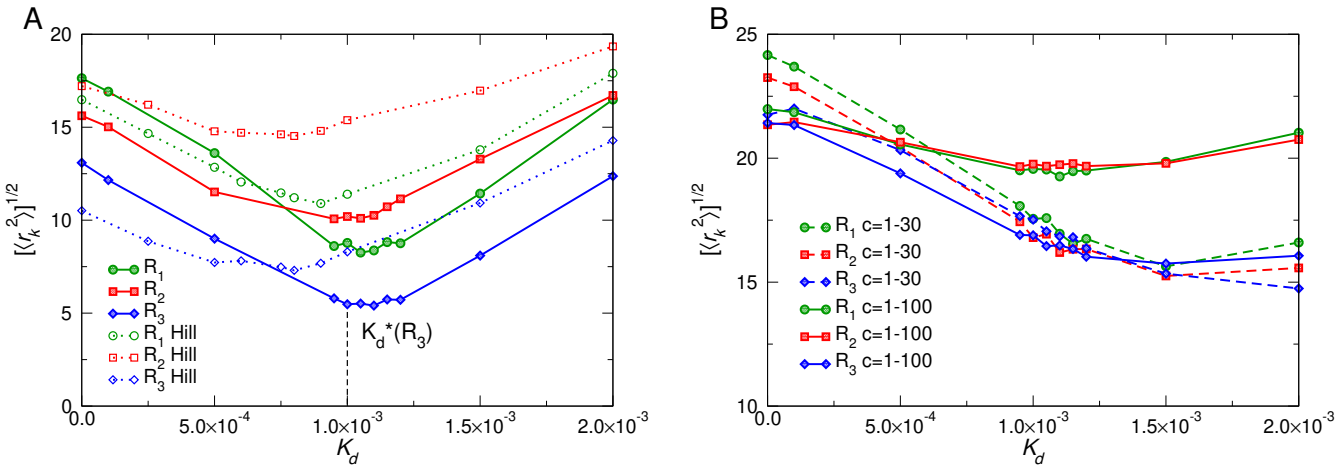

Fig. S8. RMS residual, Eq. (S26), as a function of the equilibrium dissociation rate K_d. **(A)** Solid lines: Results from the common fit of the experimental data sets $c = 1 - 10$ for the three repeats R_{1-3}. Dotted lines: Results for the Hill model with fragmentation, see Eq. (S35) and Sec. E. **(B)** Results from the common fit of the experimental data sets for $c = 1 - 30$ (dashed lines) and $c = 1 - 100$ (solid lines) for the thre repeats R_{1-3}.

For each one of the three experimental repeats R_1, R_2, R_3, we have then performed a common fit of the theoretical curves to the three experimental data sets corresponding to the densities $c = 1, 3$ and 10, in order to determine the best-fit value of τ. The experimentally measured mean filament length (in μm) has been converted to ULFs using the following relation, which takes into account the different effective length of a ULF when found along (49 nm) or at the extremity (59 nm) of a filament (1):

$$\langle L_{\mathrm{ULF}} \rangle = \frac{\langle L_{\mu\mathrm{m}} \rangle - 0.059\mu\mathrm{m}}{0.049\mu\mathrm{m}} + 1 \qquad [S23]$$

We note that, whereas fitting the three densities separately would result in three different estimates of τ, the common fit results in a single estimate of this parameter. The fit was performed using the non-linear least-squares method, implemented through the function *optimize.curve_fit* of the open-source Python library Scipy (9), which employs the Levenberg–Marquardt algorithm (10). We note that, in order to perform the fit, it has first been necessary to obtain continuous a representation of $\langle L_{\mathrm{sim}} \rangle$, so that its value could be calculated for an arbitrary t/τ. This was achieved by interpolating $\langle L_{\mathrm{sim}} \rangle$ with a cubic b-spline (11) (Scipy function *interpolate.splrep*).

The procedure described above has allowed us to find for each repeat and each K_d the value of τ which best fits the experimental data. We note that the fit has not been performed simultaneously on K_d and τ due to the fact that, whereas τ is a simple scaling factor of time, changing the value of K_d requires to perform a new simulation. In order to find the overall best-fit values of K_d and τ, for each value of K_d and for each repeat we have calculated explicitly the sum of the squared residuals (12), defined as

$$S(K_d, \tau) = \left[\sum_{k=1}^{N_1} r_k^2(1, K_d, \tau) + \sum_{k=1}^{N_3} r_k^2(3, K_d, \tau) + \sum_{k=1}^{N_{10}} r_k^2(10, K_d, \tau) \right], \qquad [S24]$$

where

$$r_k^2(c, K_d, \tau) = \left[\langle L \rangle_k - \langle L_{\mathrm{sim}}(c, K_d; t_k/\tau) \rangle \right]^2 \qquad [S25]$$

is the k-th squared residual, with $(t_k, \langle L \rangle_k)$, $k = 1, \ldots, N_c$ the experimental data points for a given density c and for the selected repeat. Each of the three functions $S(K_d, \tau)$ corresponding to R_1, R_2 and R_3 has then been minimized in order to determine the best-fit value of K_d, denoted K_d^*. The corresponding τ value is also taken as the best-fit value of τ and denoted τ^*.

Repeat	K_d^*	τ^*(h)
R_1	1.05×10^{-3}	8.32
R_2	9.50×10^{-4}	14.3
R_3	1.00×10^{-3}	17.3

Table S1. Best fit parameters K_d^* and τ^* from the common fit of the experimental data sets $c = 1, 3, 10$ for the three repeats R_{1-3} (see Fig. S8A).

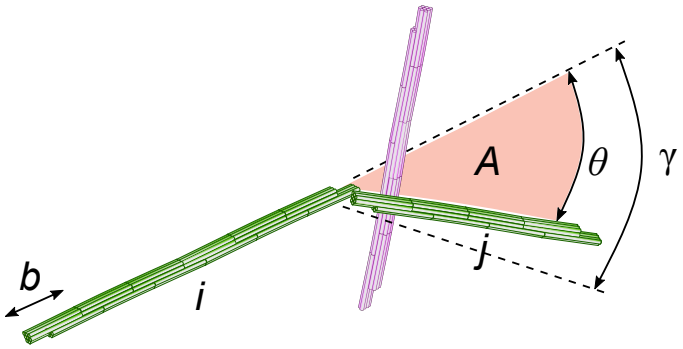

Fig. S9. Schematic represenation of an annealing reaction between two filaments of i and j ULFs (green) being blocked by a third one (purple). The size of the ULF is b, and the angle γ represents the minimum angle required for the annealing to take place. If the third filaments lies in the shaded circular sector of area $A = (bj)^2\theta/2$, the reaction is blocked.

In Fig. S8A, we show for each of the repeats R_{1-3} the root-mean-squared (RMS) residual,

$$[\langle r_k^2(c, K_d, \tau)\rangle]^{1/2} = \left[\frac{S(K_d, \tau)}{nN_{\rm tot}}\right]^{1/2}, \qquad [S26]$$

where $N_{\rm tot} = N_1 + N_3 + N_{10}$ and n is the number of densities considered (in the case of Eq. (S24), $n = 3$) . By direct inspection* of the curves, we have found for K_d^* the values that are reported in Table S1 alongside the corresponding τ^* values. We have taken the overall best-fit value of K_d (τ) as the average over the K_d^* (τ^*); the final result is $K_d = (1.00 \pm 0.05) \times 10^{-3}$ (mean $\pm$ SD). Converting this value to experimental units, one obtains $K_d = (1.00 \pm 0.05) \times 10^{-5}$ mg/mL. The corresponding value of τ is 13 ± 5 h.

In Fig. S8B we also show the functions $[\langle r_k^2(c, K_d, \tau)\rangle]^{1/2}$ obtained by performing for each repeat a common fit including the density $c = 30$ (dashed lines) and one including $c = 30$ and 100 (solid lines). One can see that the values of S obtained from to these fits are overall significantly larger than those obtained by fitting the three lowest densities. This is due to the kinetic slowing down which affects the system for $c > 10$, as it was discussed in the main text (see also Sec. D), and justifies *a posteriori* the choice of determining K_d and τ from the three lowest densities only.

D. Effect of entanglement (kinetic arrest). Comparing with the experimental data the theoretical results obtained *via* the DSMC algorithm described in Sec. B (dashed lines in Fig. 1B of the main text), one can see that the theory systematically and severely overestimates the mean filament length at equilibrium for the two highest densities ($c = 30$ and $c = 100$). We have speculated that this is due to the fact that at high density the experimental system becomes entangled, and thus the Smoluchowski description detailed in Sec. A becomes inadequate. Indeed, this theory is based on the assumption that annealing and fragmentation are purely two-body processes, which is a good approximation only in a dilute system. In a concentrated/entangled system, the presence of neighboring filament will likely hinder the annealing and fragmentation reactions. In the limit of very long filaments or very high concentrations, this will lead to a dramatic slowing down of the assembly, *i.e.* to a *kinetic arrest*. The objective of this Section is to propose a simple theoretical description of the microscopic mechanism of this slowing down. Since it would be very complex to extend the Smoluchowski theory to comprehend three-body interactions explicitly, we will adopt an "effective medium" description, in which the effect of the neighboring filaments on the annealing and fragmentation reaction is captured by a mean-field term.

Our model follows a similar approach to the one described in Ref. (13), which considers excluded volume interactions between rigid filaments undergoing bundling. In Ref. (13), all filaments are assumed to have the same length L, and to coalesce by lateral association. Here, we will assume the filaments to undergo end-to-end annealing and fragmentation as already described in Sec. A.

The microscopic mechanism that we propose for the hindering (*blocking*) of the microscopic annealing/fragmentation reactions is schematically represented in Fig. S9. In what follows, we assume that two filaments (modeled as diffusing rigid rods as detailed in Sec. A) can anneal/fragment only if the angle between them is smaller than 2γ, where γ is an adjustable parameter of the theory. We additionally assume an annealing/fragmentation reaction between two filaments of lengths (in ULFs) i, j will be blocked if at least another filament intersects the circular sector of area A. With reference to Fig. S9, one can see that

$$A = \frac{(bl_{\rm min})^2\theta}{2}, \qquad [S27]$$

where b is the ULF size and θ the angle between the two reacting filaments, and we have defined $l_{\rm min} = \min(i, j)$. The probability that a given filament of length k intersects this surface is

*A better estimate would be obtained by interpolating $S(K_d, \tau)$, or equivalently $[\langle r_k^2(c, K_d, \tau)\rangle]^{1/2}$, around the minimum with a parabola. However, as it is clear from the discussion on the error estimate, the difference between these two estimates (direct inspection and interpolation around the minimum) is negligible when compared to the error deriving from the spread of the experimental data.

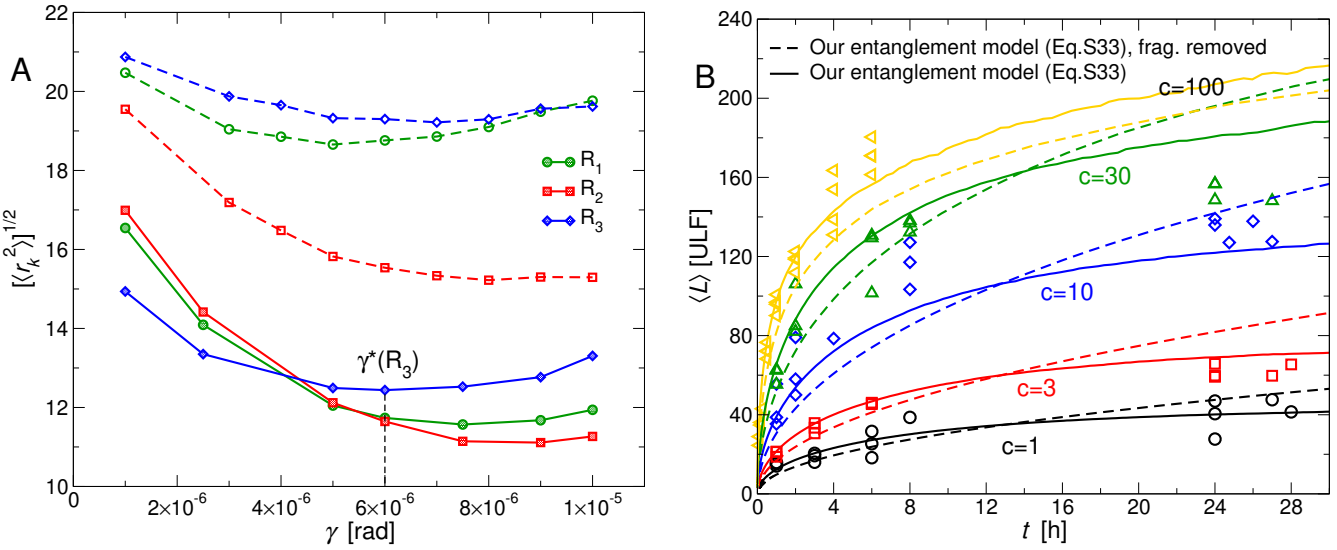

Fig. S10. (A) RMS residual, Eq. (S26), as a function of the minimum angle required for annealing γ (results from the common fit of the experimental data sets $c = 1 - 10$ for the three repeats R_{1-3}). Solid lines/filled symbols: model with fragmentation and entanglement. Dashed lines/empty symbols: model without fragmentation, with entanglement. **(B)** Fit of the experimental data. Solid lines: model with fragmentation and entanglement ($K_d = 1.0 \times 10^{-3}, \gamma = 7 \times 10^{-6}$). Dashed lines: model without fragmentation, with entanglement ($K_d = 0, \gamma = 7 \times 10^{-6}$).

$$p(A,k) = \frac{Abk}{V}, \tag{S28}$$

Thus, the probability that none of the n filaments in the system intersects the surface is, denoting the *blocking probability* with P_b,

$$1 - P_b = \prod_{k=1}^{n} \left(1 - \frac{Abk}{V}\right) \simeq \exp\left(-\frac{Ab}{V}\sum_{k=1}^{n} k\right) = \exp\left(-cbA\right), \tag{S29}$$

where c is the total concentration of ULF, and we have used the fact that $Abk/V \ll 1$ for large volumes V. The probability of Eq. (S29) was calculated for a given configuration of two filaments; thus, the average probability will be obtained by averaging over all the possible angles $0 < \theta < \gamma$ between two filaments i and j undergoing annealing:

$$1 - \langle P_b \rangle = \frac{\int_0^\gamma \exp\left(-\frac{cb^3 l_{\min}^2 \theta}{2}\right) \sin\theta \mathrm{d}\theta}{\int_0^\gamma \sin\theta \mathrm{d}\theta}. \tag{S30}$$

Solving the two integrals, we finally obtain

$$1 - \langle P_b \rangle = g\left(\frac{cb^3 l_{\min}^2}{2}, \gamma\right), \tag{S31}$$

where

$$g(x,\gamma) = \frac{1 - e^{-\gamma x}[x\sin(\gamma) + \cos(\gamma)]}{(1+x^2)[1-\cos(\gamma)]}. \tag{S32}$$

Thus, in conclusion, we propose that the annealing rate in the entangled regime is modified as follows:

$$K_{i,j}^{\mathrm{ent}} = g\left(\frac{cb^3 l_{\min}^2}{2}, \gamma\right) K_{i,j}, \tag{S33}$$

where $K_{i,j}$ is given by Eq. (S7).

To find the value of γ which best fits the experimental data, we have run DSMC simulations for different values of γ, while keeping the equilibrium dissociation constant the same as the one that was estimated by fitting the model without entanglement to the data for the three lowest densities (Sec. C). In particular, we have set $K_d = 1.0 \times 10^{-3}$, since this is the value which minimizes the sum of squared residuals when fitting the three lowest densities. The reason to keep K_d constant is that the kinetic slowing down caused by entanglement cannot modify the equilibrium properties of the system.

For each value of γ, we have run 50 independent simulations, in each one of which the random number generator was initialized with a different seed. We have then fitted the experimental data following the same procedure described in Sec. C, considering this time the whole range of concentrations, $c = 1, 3, 10, 30$ and 100. When performing this fit, K_d has been treated as a constant, with γ and τ the fit parameters. As shown by the solid lines/filled symbols in Fig. S10A, we have found that the best fit parameters, obtained by calculating the average and standard deviation over the three experimental repeats R_{1-3}, are $\gamma = (7 \pm 2) \times 10^{-6}$ rad and $\tau^* = 18 \pm 4$ h. Since we had found $K_d = (1.00 \pm 0.05) \times 10^{-3}$, we have also analyzed the effect that this 5% on K_d has on the estimates of γ and τ, finding that these do not change significantly (not shown).

Finally, it is interesting to compare the experimental data with the same model as Eq. (S33), but without fragmentation (*i.e.*, $K_d = 0$). We have thus fitted the data with this model, finding, as shown by the dashed lines/empty symbols in Fig. S10A, $\gamma = (7 \pm 2) \times 10^{-6}$ rad. The value of γ for the model without fragmentation is thus identical (within the error bars) to the one found for the model with fragmentation. However, one can see that the RMS residual is significantly higher, and thus the model without fragmentation provides a worse description of the data. This is also shown in Fig. S10B, where the fit results for the two models are compared. One can see that the model without fragmentation fails to capture especially the long-time saturation for $c < 100$, which is expected since fragmentation is more relevant at longer times.

E. Comparison with the Hill model. In this Section, we will discuss how the experimental data compare to numerical results obtained using the Hill model (14) for the annealing rate $K_{i,j}$. We find it especially relevant to discuss this model since it has been widely used for the analysis of vimentin growth kinetics (15–17). We note that all of the previous studies have assumed the absence of fragmentation, whereas here we consider the Hill model *with fragmentation*.

The Hill model assumes that the two reacting filaments can be treated as diffusing rigid rods with diffusion coefficients D_i, D_j and lengths $l_i, l_j = b \cdot i, b \cdot j$ (b = ULF size). Here $D_i \propto \ln(i) i^{-1}$: although this relation describes somewhat more accurately the diffusion of thin rigid rods than the one used in this work (4), *i.e.* $D_i \propto i^{-1}$, the two have the same asymptotic behavior for large i. Moreover, the diffusion coefficient used by Hill vanishes for reactions involving single ULFs ($i = 1$ or $j = 1$), and thus in order to perform numerical calculations using this formula one must consider corrections to the logarithmic term (15, 16). Here, following Portet *et al.* (16), we will use the following expression for D_i when discussing the Hill model:

$$D_i \propto \frac{\ln(i) + 0.312}{i}. \qquad [S34]$$

The constant 0.312 is a zero-order correction in i^{-1} for the diffusion coefficient of short filaments (18). In the Hill model, two filaments that are at a distance $r_{i,j} < (l_i + l_j)/2$ from each other will react with probability $p_{i,j}$. This probability is evaluated by Hill as the fraction of surface of the sphere of radius $r_{i,j}$ which is reactive. Since the area of the reactive site is $\approx b^2$, one obtains $p_{i,j} \propto b^2 / r_{i,j}^2 \propto (i + j)^{-2}$. As we discuss below, this leads to a faster decrease of the reaction rate with filament length compared to our model. The reaction rate of Hill is thus

$$K_{i,j}^H = (D_i + D_j) \frac{l_i + l_j}{2} p_{i,j} = C \left[\frac{\ln(i) + 0.312}{i} + \frac{\ln(j) + 0.312}{j} \right] (i + j)^{-1}, \qquad [S35]$$

where C does not depend on i, j nor on density.

We have performed DSMC simulations of the Smoluchowski equation with fragmentation, as described in Secs. A-B, with the annealing rate given by Eq. (S35). We recall that the fragmentation rate is derived from the detailed balance condition, Eq. (S1). The simulations have been performed for the reduced densities $c = 1, 3, 10$, corresponding to the three lowest experimental densities, and for different values of the equilibrium dissociation constant K_d. For each value of c and K_d, we have run 50 independent simulations by initializing the random number generator with different seeds. In order to determine the best-fit value K_d^* and the associated mean fragmentation time τ^*, we have followed the same procedure described in Sec. C. For the best fit values, we find $K_d^* = (8.0 \pm 0.8) \cdot 10^{-4}$ and $\tau^* = 24 \pm 9$ h. The Hill model thus predicts a slightly smaller but comparable equilibrium dissociation constant and a mean bond breaking time which is approximately double the one predicted by our model, Eq. (S7).

In Fig. S8 we show the RMS residual from the fit, Eq. (S26) (dotted lines, empty symbols), compared to the same quantity obtained with our model (solid lines, filled symbols). One can see by comparing the two curves that fitting the experimental data with the Hill model results in a larger value of the RMS residual in the range of K_d around the minimum K_d^*.

The fit is shown in Fig. S11A, where it is compared with the one obtained with our model. We note that the Hill model predicts a slower filament growth at short and intermediate times. This can be understood as follows: If one replaces for simplicity i and j with a single typical length L in Eq. (S35), it is easy to see that for intermediate/long filaments thereaction rate scales as $K \propto L^{-2}$. In our model, Eq. (S7) , on the other hand, the scaling is $K \propto L^{-1}$. Thus, the Hill model predicts a faster decrease of the reaction rate with increasing filament length.

It can actually be shown that, in the absence of fragmentation, a scaling $K \propto L^{-\lambda}$ leads to an increase of the mean filament length with time as $L(t) \propto t^{1/(1+\lambda)}$ (19). This results in $L(t) \propto t^{1/2}$ for our model and $L(t) \propto t^{1/3}$ for the Hill model. These two regimes are indeed observed at short/intermediate times, when fragmentation is less relevant, as shown in Fig. S11B, where we show the same data as in Fig. S11A in double-logarithmic scale. From this plot, one can clearly see that at short/intermediate times the experimental data follow a slope much closer to the value 1/2 predicted by our model than to the 1/3 predicted by the one of Hill. We thus conclude that our model captures the assembly kinetics of vimentin better than the one of Hill.

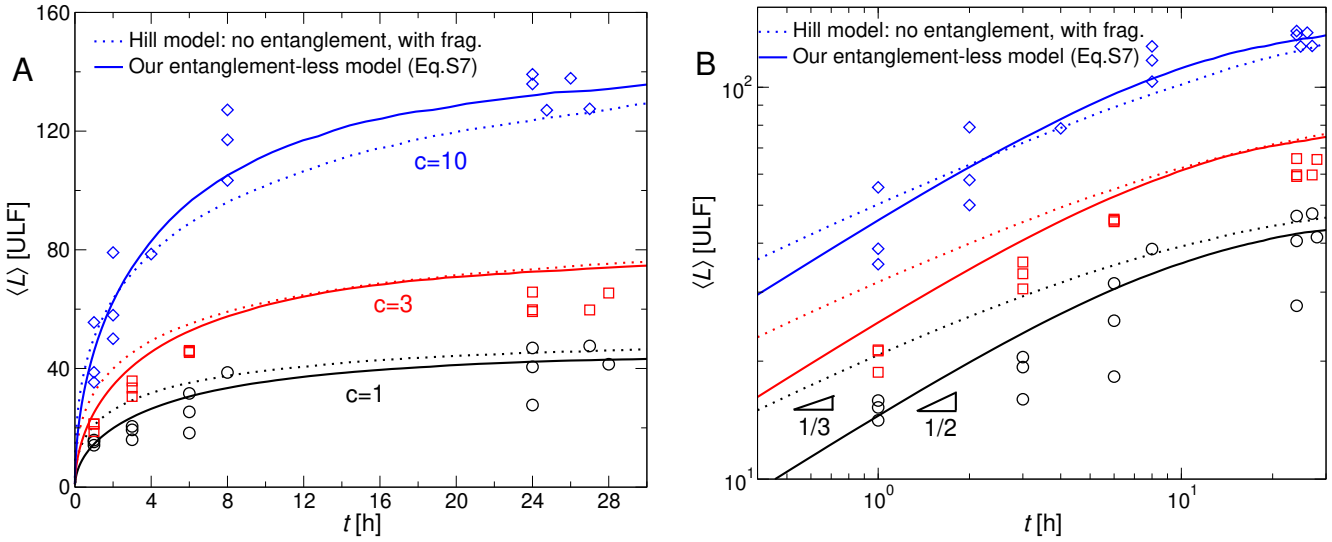

Fig. S11. (A) Fit of the experimental data (symbols) obtained using our model for the annealing rate, $K_{i,j} = K_{1,1}(i^{-1} + j^{-1})/2$ (solid lines), and the Hill model with fragmentation (Eq. (S35), dashed lines). **(B)** Same data as in (A) in double-logarithmic scale. For our model, $K_d = 1.00 \times 10^{-3}$, $\tau = 13$ h. For the Hill model, $K_d = 8.0 \times 10^{-4}$, $\tau = 24.0$ h. Note that all the data shown in A-B are for models *without entanglement*, as the latter are not relevant in this range of densities.

Material and Methods

In vitro reconstitution of vimentin wild-type. We purified vimentin wild-type protein from *E. coli* bacteria as described previously (20). In short, vimentin wild-type was expressed in BL21 star (Sigma-Aldrich) cultured in Terrific Broth medium overnight at 37 °C, after induction at a DO of 1.2. We then centrifuged the culture medium to obtain the bacteria, then lysed them with lysozyme in the presence of DNase (Roche), RNase (Roche) and protein inhibitors (pefabloc and PMSF). We collected the inclusion bodies, washed them 5 times by successive steps of centrifugation and resuspension using a cooled douncer. After the last washing step, inclusion bodies were resuspended in a denaturing buffer (8 M urea, 5 mM Tris pH 7.5, 1 mM EDTA, 1 mM DTT, 1 % PMSF) and centrifuged at high speed (100 000 × g) for 1 h. After collecting the supernatant, we conducted vimentin purification after two steps of exchange chromatography, using first an anionic (DEAE Sepharose, GE Healthcare) then a cationic (CM Sepharose, GE Healthcare) column. The vimentin protein was collected in 2 mL Eppendorf tubes, and the concentration was monitored by Bradford. Only the most concentrated fractions were selected and mixed together. We stored the vimentin at -80 °C with additional 10 mM methylamine hydrochloride solution.

To obtain vimentin wild-type proteins for experiment, the denatured proteins were transferred to a dialysis tubing (Servapor, cut off at 12 kDa) and renatured by stepwise dialysis from 8 M, 6 M, 4 M, 2 M, 1 M, 0 M urea into sodium phosphate buffer (2.5 mM, pH 7.0, 1 mM DTT) with 15 minutes for each step. The final dialysis step was performed overnight at 4 °C with 2 L of the sodium phosphate buffer.

Labeling of wild-type vimentin. We labeled our vimentin proteins fluorescently through their single cysteine following a protocol that was described previously (21). In details, denatured wild-type vimentin in 8 M urea was dialyzed for 3 h in a buffer containing sodium phosphate 50 mM, pH 7.0 and 5 M urea. Then, fluorescence dye (either AF-488 C5 maleimide or AF-555 C2 maleimide) in DMSO was added to the vimentin to a final concentration of 0.8 mg · mL^{-1}, and mixed gently for 1 h. The reaction was then quenched by addition of 1 mM DTT. The excess dye was removed from the mixture using a Dye Removal Column (#22858, ThermoFisher). Vimentin collected after the dye removal was renatured by stepwise dialysis from 8 M, 6 M, 4 M, 2 M, 1 M, 0 M urea to sodium phosphate buffer (2.5 mM, pH 7.0, 1 mM DTT). Renatured vimentin tetramers were stored at 4 °C for up to a week. It has been shown that fluorescent labeling impacts the assembly of vimentin (21). In our experiment, we also notice a difference in kinetics of vimentin assembly between two fluorescence dyes, AF-488 and AF-555, as shown in Fig. 4C in the main text.

Assembly assays and sample fixation for imaging. For assembly of fluorescence-labeled vimentin filaments, non-labeled vimentin wild-type tetramers were first mixed with AF-488-labeled tetramers in sodium phosphate buffer (2.5 mM, pH 7.0) to desired concentrations of 0.01, 0.03, 0.1, 0.3 and 1.0 mg mL^{-1} with a labeling rate of 20 %. The assembly was initiated by addition of KCl to the final concentration of 100 mM. Incubation was performed at 37 °C for up to 28 h using a thawing water bath (Julabo Corio C, Seelbach, Germany). During the assembly, samples were taken from assembly solutions, then fixed with an equal volume of glutaraldehyde 0.5 % in the assembly buffer (2.5 mM sodium phosphate, pH 7.0, 100 mM KCl). In particular, for the high concentration of 0.1, 0.3 and 1.0 mg mL^{-1}, samples were first diluted in the assembly buffer at ratio 1:10, 1:20 and 1:100, respectively, then fixed with an equal volume of glutaraldehyde 0.5 % in the assembly buffer. Similar to labeled filaments, non-labeled filaments were assembled at 0.01 mg mL^{-1} at 37 °C for a duration up to 33 h in the assembly buffer. During the assembly, small samples were taken at different time points, then fixed with an equal volume of glutaraldehyde

0.5 % in the assembly buffer. The fixed samples were then ready for imaging.

Dilution experiment. We used vimentin labeled in AF-488 with 20 % fluorescence labeling rate and conducted the assembly at initial concentration 0.2 mg mL^{-1} for 2 h and 1.0 mg mL^{-1} for 30 minutes, at 37 °C. Assembled filaments were then diluted at different ratios, from 1:10 to 1:1000 in the assembly buffer. We continued to incubate the diluted sets of filaments at 37 °C for another 6 h. Samples for imaging were taken every 1-2 hours.

Dual color experiment. We prepared two separate sets of vimentin, both at the same concentration 0.2 mg mL^{-1}, but labeled in two different colors: one with AF-488 (green) and the other one with AF-555 (red). Both have the same 20 % fluorescence labeling rate. We conducted the assembly of the two sets for 3 hours at 37 °C. Then, we mixed the two sets of filaments together (mixing ratio 1:1), and continued to incubate the mixture at 37 °C for another 6 h. Samples for imaging were taken every 2 h.

Fluorescence microscopy imaging. We transferred 3 µL of fixed vimentin filaments labeled with AF-488 or AF-555 onto a glass slide and put on a coverslip. The samples were then observed using an inverted microscope (Nikon Eclipse T*i*) and imaged using an sCMOS camera (C11440-42U30, Hamamatsu Photonics, Japan).

Transmission electron microscopy imaging. We pipetted 4 µL of each fixed sample onto a carbon coated grid primarily glow discharged and incubated it at room temperature (25 °C) for one minute. Then, we performed negative staining by injecting 2 % uranyl acetate in water to contrast the grids and continue to incubate for one minute. The grids were then air-dried and observed under 120 kV using a Tecnai microscope (Thermofisher) and imaged using a 4k×4k Eagle camera (Thermofisher).

Filament length analysis. Length quantification of vimentin filaments imaged in fluorescence microscopy and electron microscopy were conducted manually using Fiji. Only filaments above 0.5 µm length were considered for analysis in the fluorescence microscopy experiments.

References

1. FN Vicente, et al., Molecular organization and mechanics of single vimentin filaments revealed by super-resolution imaging. *Sci. Adv.* **8**, eabm2696 (2022).
2. P Van Dongen, M Ernst, Kinetics of reversible polymerization. *J. Stat. Phys.* **37**, 301–324 (1984).
3. F Sciortino, C De Michele, JF Douglas, Growth of equilibrium polymers under non-equilibrium conditions. *J. Phys.: Condens. Matter* **20**, 155101 (2008).
4. M Doi, SF Edwards, *The theory of polymer dynamics.* (Oxford university press), (1986).
5. OG Berg, PH von Hippel, Diffusion-controlled macromolecular interactions. *Annu. Rev. Biophys.* **14**, 131–158 (1985).
6. AL Garcia, C Van Den Broeck, M Aertsens, R Serneels, A monte carlo simulation of coagulation. *Phys. A* **143**, 535–546 (1987).
7. K Liffman, A direct simulation monte-carlo method for cluster coagulation. *J. Comput. Phys.* **100**, 116–127 (1992).
8. FE Kruis, A Maisels, H Fissan, Direct simulation monte carlo method for particle coagulation and aggregation. *AIChE J.* **46**, 1735–1742 (2000).
9. P Virtanen, et al., Scipy 1.0: fundamental algorithms for scientific computing in python. *Nat. Methods* **17**, 261–272 (2020).
10. JJ Moré, The levenberg-marquardt algorithm: implementation and theory in *Numerical analysis.* (Springer), pp. 105–116 (1978).
11. P Dierckx, An algorithm for smoothing, differentiation and integration of experimental data using spline functions. *J. Comput. Appl. Math.* **1**, 165–184 (1975).
12. WC Hamilton, *Statistics in physical science: Estimation, hypothesis testing, and least squares.* (New York: Ronald Press Co.), (1964).
13. G Foffano, N Levernier, M Lenz, The dynamics of filament assembly define cytoskeletal network morphology. *Nat. Commun.* **7**, 1–8 (2016).
14. TL Hill, Length dependence of rate constants for end-to-end association and dissociation of equilibrium linear aggregates. *Biophys. J.* **44**, 285–288 (1983).
15. S Portet, et al., Vimentin intermediate filament formation: in vitro measurement and mathematical modeling of the filament length distribution during assembly. *Langmuir* **25**, 8817–8823 (2009).
16. S Portet, Dynamics of in vitro intermediate filament length distributions. *J. Theor. Biol.* **332**, 20–29 (2013).
17. CG Lopez, O Saldanha, K Huber, S Köster, Lateral association and elongation of vimentin intermediate filament proteins: A time-resolved light-scattering study. *Proc. Natl. Acad. Sci.* **113**, 11152–11157 (2016).
18. JG De La Torre, C Lopez, Dimensions of short, rodlike macromolecules from. *Biopolymers* **23**, 611–615 (1984).
19. P Meakin, MH Ernst, Scaling in aggregation with breakup simulations and mean-field theory. *Phys. Rev. Lett.* **60**, 2503 (1988).
20. H Herrmann, L Kreplak, U Aebi, Isolation, characterization, and in vitro assembly of intermediate filaments. *Methods Cell Biol* **78**, 3–24 (2004).
21. S Winheim, et al., Deconstructing the late phase of vimentin assembly by total internal reflection fluorescence microscopy (tirfm). *PloS one* **6**, e19202 (2011).